Title	Experimental study of tunneling phenomena in submicroscale magnetic systems
Author(s)	田中, 崇大
Citation	大阪大学, 2016, 博士論文
Version Type	VoR
URL	https://doi.org/10.18910/56090
rights	
Note	

Dissertation for Doctoral Degree

Experimental study of tunneling phenomena in submicroscale magnetic systems

Department of Physics, Graduate School of Science, Osaka University

Takahiro Tanaka

2016

Abstract

The tunnel effect is one of the most fundamental phenomena in quantum mechanics. This effect plays an important role in several physical phenomena such as the cosmic inflation and the alpha decay. It is also of significance in solid state physics as we see in the tunnel diode and scanning tunneling microscope.

In this thesis, we focus on the tunnel effect in the ferromagnet and the ferromagnetic device, where the spin-dependent tunnel effect and the tunnel effect of spin degree of freedom are expected. We measured the shot noise in the magnetic tunneling junctions (MTJs), which are one of the most fascinating tunnel devices. The shot noise measurement is a useful tool for studying the electron transport in the tunnel junctions beyond the dc measurement and enables us to clarify further the tunneling process. We are also interested in the macroscopic quantum tunneling in the magnetic vortex. It requires the detection of the magnetic vortex core. We investigate a possible method of the detection by the billiard simulation.

In Chapter 1, the tunnel effect in solid state and the current noise are explained. First, the tunnel effect in one dimension and transport in a tunnel junction are explained. Next, we introduce the tunnel magnetoresistance (TMR) effect in the MTJs and the mechanisms of the TMR effect, which are called Jullière model and coherent tunnel model. The macroscopic quantum tunneling is briefly described. Finally, we explain the three types of the current noise, namely the thermal noise, shot noise and $1/f$ noise, as well as the Fano factor, which characterizes the shot noise.

In Chapter 2, we describe the measurement setup and the analysis method for evaluating the current noise.

In Chapter 3, we discuss the coherent tunnel in the MTJs with the spinel $MgAl_2O_4$ barrier. We describe the previous study of the shot noise in MTJs with MgO barrier and discuss the relevance between the shot noise and coherent tunnel. In our experiment, the spin-dependent suppression of the shot noise is confirmed. This result suggests that the coherent tunnel is essential to understand the transport in $MgAl_2O_4$-based MTJs.

In Chapter 4, we discuss the microscopic tunnel process in MgO-based MTJs. In MTJs, there also exist other transport processes caused by the sequential tunneling or the leak current due to the pinhole and the photon assisted tunneling. We estimate the

contribution of the leak current due to the pinhole by means of the shot noise measurement.

In Chapter 5, we describe the detection method of the magnetic vortex core by using microcavity fabricated on two dimensional electron gas. By the billiard simulation, it is found that the microcavity can detect the magnetic vortex core in principle.

Finally, we summarize this thesis in Chapter 6.

Contents

Chapter 1

Introduction

1.1 Tunnel effect

1.1.1 Tunnel effect in solid state [1]

In quantum physics, there are many phenomena beyond the classical concepts. The tunnel effect is a typical phenomenon appearing in quantum physics. The conventional tunnel effect is a phenomenon that microscopic particles can pass through a potential barrier higher than their kinetic energy. It is caused by the seeping of wave function from the one side to the other of a potential barrier. This tunnel effect is observed in the whole area of quantum physics and plays important roles. The alpha decay, which is one of the radioactive decay, is the first example where the idea of tunnel effect was applied. These days, this idea ranges even to the beginning of the universe. In solid-state physics, the study of the tunnel effect began from the field emission of electrons at a surface of a metal. Later, the tunnel effect has been intensively studied especially in the fields of semiconductor and superconductor such as the tunnel (Esaki) diode [2] and Josephson effect [3]. L. Esaki, I. Giaever and B. D. Josephson won the Nobel prize in 1973 [2–4]. Remarkably, it was also found that the macroscopic quantum variable with a numerous degree of freedom such as the phase of the superconductor can tunnel as well as the microscopic variable, which receives a lot of attention [5]. In this section, we describe the tunnel effect in a one dimensional system and the transport in the tunnel junction. Later, we explain magnetic tunnel junction which is one of the most attractive tunnel devices [6]. Finally, we introduce the macroscopic quantum tunneling.

Tunnel effect in one dimensional box-type potential

First, we consider the tunnel effect in the one dimensional box-type potential, where we

can obtain the exact solution. This potential is expressed as

$$U(x) = \begin{cases} 0 & (x < 0) \\ U_0 & (0 < x < a) \\ 0 & (a < x) \end{cases} \tag{1.1}$$

as shown in Fig. 1.1. We consider only the case that the energy of the electron $E > 0$ is smaller than the height of the box-type potential $U_0 > 0$, where the tunnel effect is the most remarkable. We can obtain the tunnel probability T by solving the Schrödinger equation

$$\left(-\frac{\hbar^2}{2m} \frac{d^2}{dt^2} + U(x) \right) \psi = E\psi. \tag{1.2}$$

The result of the tunnel probability is written as

$$T = \frac{4\varepsilon(1-\varepsilon)}{4\varepsilon(1-\varepsilon) + \sinh^2(\eta\sqrt{1-\varepsilon})}. \tag{1.3}$$

Here, $\varepsilon = \frac{E}{U_0}$ and $\eta = \sqrt{2mU_0a^2}/\hbar$. Figure 1.2 shows the energy dependence of the tunnel probability for $\eta = 4$. T increases monotonously with increasing energy of the electron.
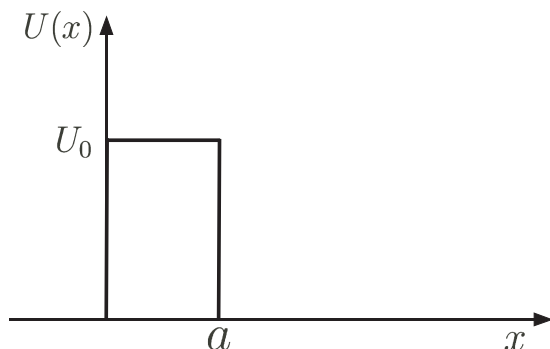
Figure 1.1: The shape of the box-type potential.
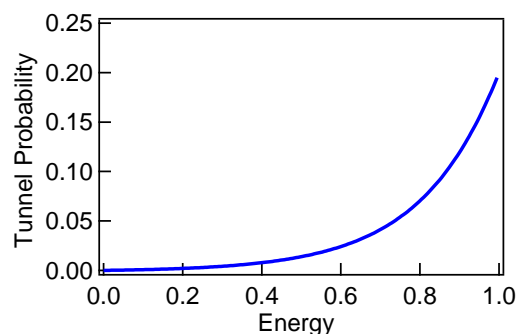
Figure 1.2: Energy dependence of the tunnel probability for $\eta = 4$.

Conductance in tunnel junction

In the above, we saw that the tunnel probability is depending on the energy of the electron. In the three dimensional conductor, electrons with the same energy may have different wave number vector $\boldsymbol{k}$ and the tunnel probability depends on $\boldsymbol{k}$. Here, we show that the conductance of a tunnel junction can be expressed by Landauer formula, which relates the conductance to the tunnel probability [7]. We consider two reservoirs for electrons R_L and R_R with chemical potential μ_L and μ_R, respectively, connected by a tunnel barrier as shown in Fig. 1.3 [9]. One electron with the velocity for the direction from the left

reservoir to the right reservoir (z direction) v_z^+ carries a current equal to ev_z^+. We can write the current density of electrons which leave R_L and enter R_R such that

$$J^+ = \frac{2e}{(2\pi)^3} \int d^3k v_z^+(\boldsymbol{k}) f^+(E) T(\boldsymbol{k}) = \frac{2e}{A} \sum_{k_\parallel, j,} \frac{1}{2\pi} \int dk_z \frac{1}{\hbar} \frac{\partial E}{\partial k_z} f^+(E) T(\boldsymbol{k}), \qquad (1.4)$$

where we use a relation $v_z^+ = \frac{1}{\hbar} \frac{\partial E}{\partial k_z}$. $k_\parallel$ is the wave number parallel to the tunnel barrier, j is the Bloch state of each electron, $T(\boldsymbol{k}) = \sum_{\boldsymbol{k}'} T(\boldsymbol{k}, \boldsymbol{k}')$ represents sum of the tunnel probability from $\boldsymbol{k}$ state in the left reservoir to all of $\boldsymbol{k}'$ state in the right reservoir and A is the junction area of the tunnel junction. This equation yields an expression for the tunnel current

$$I^+ = \frac{2e}{h} \int^{\mu_1} dE \sum_{k_\parallel, j} T(k_\parallel, j). \qquad (1.5)$$

We can deduce an expression for the current of electrons which leave R_R and enter R_L in the same way

$$I^- = \frac{2e}{h} \int^{\mu_2} dE \sum_{k_\parallel, j} T(k_\parallel, j). \qquad (1.6)$$

The net current is given by

$$I = I^+ - I^- = \frac{2e}{h} \int_{\mu_2}^{\mu_1} dE \sum_{k_\parallel, j} T(k_\parallel, j) = \frac{2e^2}{h} \sum_{k_\parallel, j} T(k_\parallel, j) \frac{\mu_1 - \mu_2}{e}. \qquad (1.7)$$

The two currents I^+ and I^- of those electrons whose energies are smaller than μ_2 are canceled out. We can obtain the Landauer formula

$$G = \frac{2e^2}{h} \sum_{k_\parallel, j} T(k_\parallel, j). \qquad (1.8)$$

We can regard the transport in a tunnel junction as a parallel circuit of virtually countless conducting channels with different $k_\parallel$ and j.
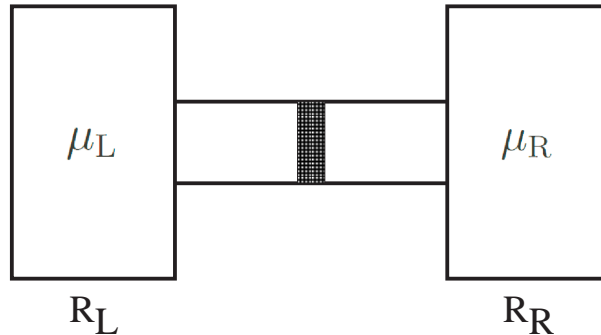

Figure 1.3: Two electron reservoirs connected by a tunnel barrier.

1.1.2 Magnetic tunneling junctions

The magnetic tunneling junctions (MTJs) attract a great deal of interest not only because MTJs offer us a suitable stage to address spin-dependent transport, but also because MTJs have enormous potential in various applications such as read head of magnetic recording medium, nonvolatile memory (STT-MRAM) and spin torque oscillator. In this section, we briefly review the history of MTJ study and explain the two important models for the mechanism of MTJs, namely Jullière model [8] and coherent tunneling model [9, 10].

MTJs consist of ferromagnet/thin insulator/ferromagnet and the resistance of MTJs changes depending on the relative alignment of two ferromagnetic layers as shown in Fig. 1.4, which is called tunneling magnetoresistance (TMR) effect. When the relative alignment is in the parallel (P) configuration, the resistance is smaller than that in the anti-parallel (AP) configuration. Magnetoresistance (MR) ratio which characterizes TMR effect is defined as

$$\text{MR ratio} \equiv \frac{R_{\text{AP}} - R_{\text{P}}}{R_{\text{P}}} \times 100 (\%) \tag{1.9}$$

by using resistance for the P configuration R_{P} and that for the AP configuration R_{AP}.

MTJs were first reported in 1975 by Jullière. He fabricated Fe/Ge-O/Co junction and observed TMR effect with MR ratio of 14 % at 4.2 K [8]. However, MTJs had not attracted attention for more than a decade because this effect was small and observed only in the low temperature. In 1987, the giant magnetoresistance (GMR) effect was discovered in ferromagnet/nonmagnetic metal multilayer [11, 12]. The structure of the GMR device corresponds to the structure of MTJs whose insulator is replaced by a nonmagnetic metal. The GMR effect, where the resistance of multilayer depends on the relative alignment of ferromagnetic layers, is similar to the TMR effect. This discovery invoked renewed interest in the TMR effect and expectation that the larger MR ratio would be observed in MTJs.

The TMR effect at room temperature was first demonstrated in an Fe/amorphous Al-O/Fe junction in 1995 by Miyazaki *et al.* [13] and Moodera *et al.* [14]. Since then, amorphous Al-O based MTJs had been studied actively and MR ratio improved up to 70 %. Although Larger MR ratio would be desirable for applications, this value of MR ratio gives the upper limit expected from a phenomenological description explained below.

In 2001, Butler *et al.* predicted by using the first principles calculation that MTJs with crystalline MgO barrier will show an MR ratio larger than 1,000 % [9, 10], where the coherent tunneling plays an important role as described below. Later in 2004, the epitaxial Fe/MgO/Fe based MTJs were fabricated by Yuasa *et al.* [15] and Parkin *et al.* [16] and they reported that MR ratio reached 180 % at room temperature [15, 16]. This value is more than twice as large as the MR ratio of Al-O based MTJs and the MR ratio continues to be enhanced. MTJs is actually applied to the read head of HDD and it enables high density recording.
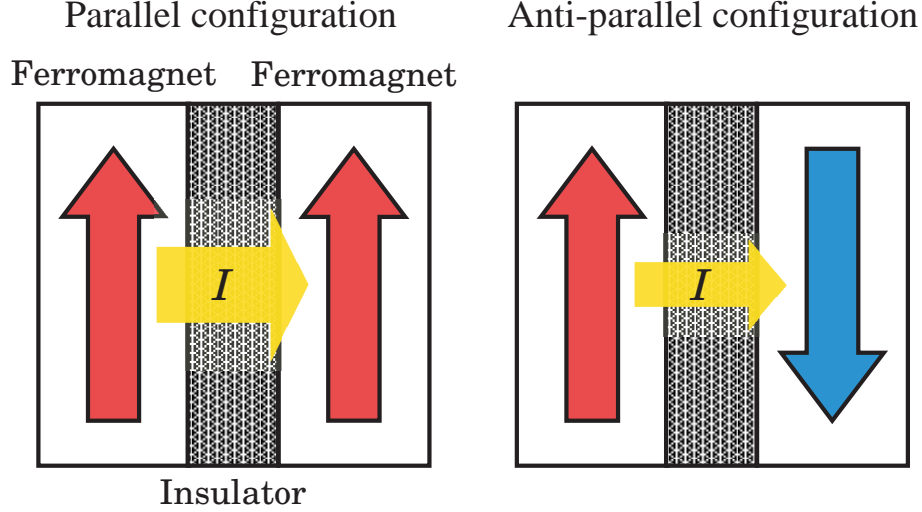
Figure 1.4: Schematic illustration of the tunneling magnetoresistance effect in a magnetic tunnel junction.

The coherent tunneling is considered to enhance the TMR effect of MTJs not only with an Fe electrode but also with Co, CoFe alloy, FePt and Co-based Heusler alloys electrodes [17–19] and MgO-based MTJs with these electrodes are actively explored. However, the lattice mismatch between MgO and these materials is relatively large (more than a few %) and the misfit dislocations are induced in the interfaces between MgO and electrodes. The spinel $MgAl_2O_4$ barrier is an alternative barrier for the coherent tunneling and the lattice mismatch between $MgAl_2O_4$ and these materials are smaller than that of MgO. Actually, the large TMR effect was reported in Fe/$MgAl_2O_4$/Fe MTJs [20, 21]. In this thesis, we address the coherent tunneling in the spinel-based MTJs in Chapter 3.

Jullière model [8]

The Jullière model describes the spin-dependent transport in MTJs phenomenologically. In this model, we consider the spin-dependent band structures of two ferromagnetic layers as shown in Fig. 1.5. It is assumed that the electron spins are conserved during tunneling processes; up (down) spins in the source ferromagnetic electrode transport into the band of up (down) spin in the drain ferromagnetic electrode. It is also assumed that all the electrons have the same tunneling probability. From these assumptions, it is found that the conductance of MTJs is proportional to $D_{1\uparrow}(E_F)D_{2\uparrow}(E_F) + D_{1\downarrow}(E_F)D_{2\downarrow}(E_F)$, where $D_{1(2)\uparrow(\downarrow)}(E_F)$ is the density of states of up (down) spin in the source (drain) ferromagnetic electrode at Fermi energy. The MR ratio is expressed by using the spin polarization of conduction electrons P_α ($\alpha = 1, 2$)which is defined as follows;

$$\text{MR ratio} = \frac{2P_1P_2}{1 - P_1P_2} \tag{1.10}$$

and

$$P_\alpha = \frac{D_\alpha \uparrow (E_\mathrm{F}) - D_\alpha \downarrow (E_\mathrm{F})}{D_\alpha \uparrow (E_\mathrm{F}) + D_\alpha \downarrow (E_\mathrm{F})} \quad (\alpha = 1, 2) \tag{1.11}$$

This model can well explain the TMR effect in amorphous Al-O based MTJs. P of $3d$ transition metallic ferromagnets and alloys composed of these ferromagnets range between 0 and 0.6 at low temperature [22] and the resultant MR ratio is expected to be at most 100 % in Jullière model. At room temperature the spin polarization becomes smaller and the MR ratio is likely to be at most 70 %. On the other hand, TMR effect in MgO-based MTJs is much larger than this expected value. We explain this mechanism below.
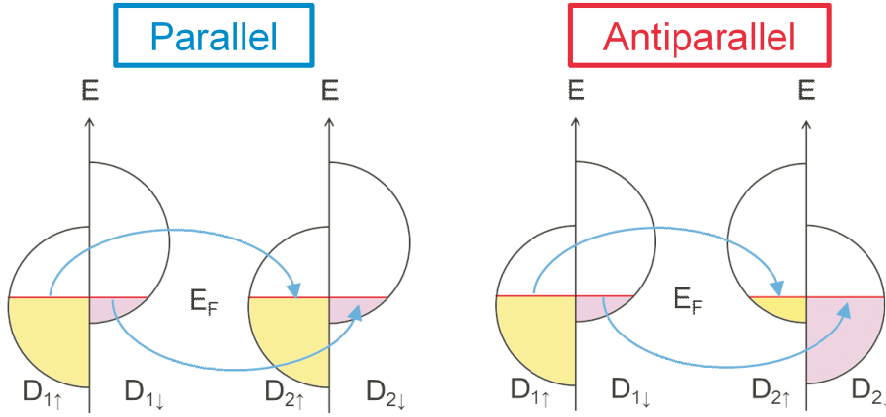

Figure 1.5: Schematic illustration of the tunneling magnetoresistance effect based on the spin-dependent density of states [6].

Coherent tunneling model [9, 10]

The large TMR effect in MgO-based MTJs can be understood in the coherent tunneling model rather than the Jullière model. The coherent transport in a tunnel junction is expressed by the Landuer formula as described in Sec. 1.1. Here "coherent" means that electrons conserve not only spin but also wave number vector. Taking the spin degree of freedom into account, we can write the conductance of MTJs from Landuer formula,

$$G = \frac{2e^2}{h} \sum_{k_\parallel, j, \sigma} T(k_\parallel, j, \sigma). \tag{1.12}$$

Here, $k_\parallel$ is the wave number parallel to the tunnel barrier, j represents the Bloch state of electrons and σ is the electron spin. In the $3d$ transition metallic ferromagnet, there are three types of Bloch state.

- Δ_1 state: It is the *spd* hybrid orbital and highly polarized at the Fermi energy as shown Fig. 1.6 [6].

6

- Δ_5 state: It is the *pd* hybrid orbital.

- Δ_2 state: It is the *d* orbital and negatively spin polarized.

These three Bloch states have different symmetry. In amorphous Al-O barrier, they are mixed by the scattering, which results in a averaged tunnel probability. Thus, the net spin polarization of tunneling electrons is the averaged value of these three Bloch states. In contrast, in MgO barrier case, electrons conserve their symmetry during the tunneling processes because of the periodic potential of crystalline MgO. Electrons in different Bloch states have different tunnel probabilities depending on their symmetries. The Δ_1 Bloch state with high symmetry has much larger tunnel probability than Δ_5 and Δ_2 Bloch states with low symmetry. The high spin polarization and tunnel probability of Δ_1 Bloch state results in the high spin polarization of conducting electrons. It leads to the large TMR effect.
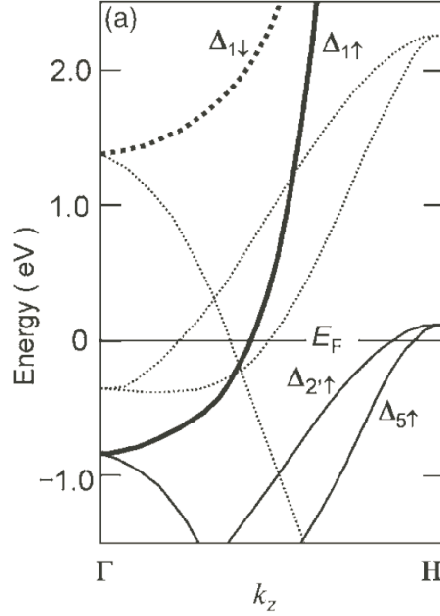
Figure 1.6: Band dispersion of bcc Fe in the [001 (Γ-H)] direction [6].

Figures 1.8(a), 1.8(b) and 1.8(c) show the tunnel probability in eight layer thick MgO barrier as a function of $k_\parallel$ for spin majority-majority channel, majority-minority channel and AP configuration respectively. For the P configuration, the conductance equals to the sum of majority-majority and minority-minority channels contribution. For the majority-majority channel, tunnel probability is much larger than that for the minority-minority channels and there is a large peak around $k_\parallel = 0$ due to the Δ_1 Bloch state. For the minority-minority channels and AP configurations, the conductance is carried not by Δ_1 Bloch state but by Δ_5 and Δ_2 Bloch states. These two wave functions are anisotropic

7
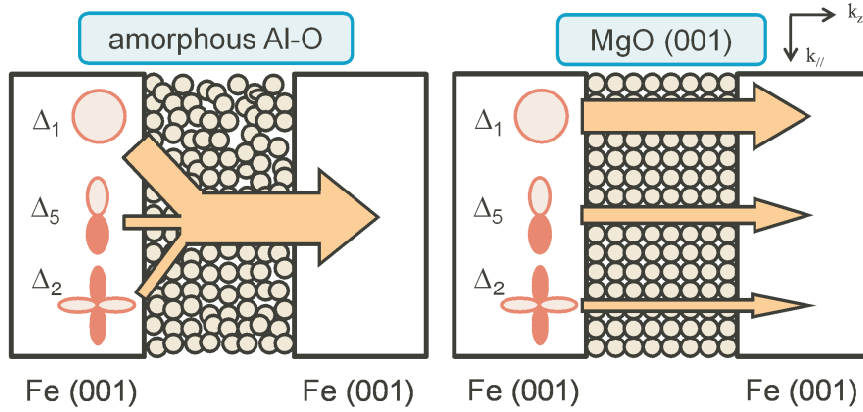
Figure 1.7: Schematic illustrations of electron tunneling through (a) an amorphous Al-O barrier and (b) a crystalline MgO (001) barrier [6].

and seep little into MgO barrier. As a result, the tunnel probability around $k_{\parallel} = 0$ is suppressed and the conductance becomes small.

As described above, the coherent tunnel is essential to the large TMR effect. Actually, the coherent tunneling was confirmed experimentally in MgO-based MTJs [23, 24]. Recently, MTJs not only with MgO barrier but also with $MgAl_2O_4$ barrier were reported, where the coherent tunneling is considered to be important [20, 21]. However, the coherent tunneling in $MgAl_2O_4$-based MTJs was not proved experimentally. In Chapter 3, we will discuss the coherent tunneling in this system by means of the noise measurement.

Figure 1.8: Tunneling probability in a Fe/eight layers of MgO/Fe MTJ as a function of k_x and k_y for (a) majority spin channels (b) minority spin channels and (c) AP configuration [9].

1.1.3 Macroscopic quantum tunneling [1, 25, 26]
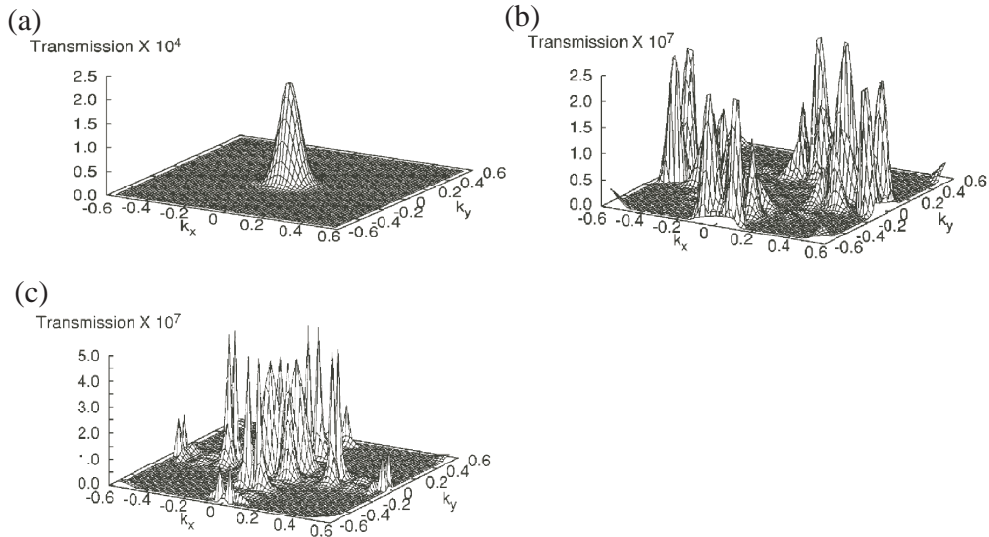
In general, the tunnel effect is considered to be observed in the microscopic scale. However, it was found that a macroscopically distinguishable physical quantity such as the phase of a superconductor can tunnel, which is called the macroscopic quantum tunneling (MQT). We saw that the wave nature is important for the tunnel effect. The scale where we can observe this wave nature is approximately de Broglie wavelength which ranges from a few angstroms (electrons in a metal) to a few hundreds angstrom (electrons in a semiconductor) in solid state. Thus the quantum effect including the tunnel effect is limited in the microscopic scale. At very low temperature, however, the situation is different when macroscopic quantum phenomena such as the superconductivity as superfluidity are observed.

First, the MQT is investigated in a superconductor [27,28] and one of the most famous MQTs is the tunnel of the magnetic flux in a superconducting quantum interference device (SQUID) [29,30]. The magnetic flux in a SQUID cannot take arbitrary values and is fixed to $\Phi = n\Phi_0$, where $\Phi_0 = h/2e$ is called quantized magnetic flux. It is caused by the fact that the phase of the order parameter which describes a superconductor must take a same value after going round the ring. This magnetic flux in a SQUID is controlled by applying the external magnetic field and we can equalize the energy of the two states with different magnetic flux. In this situation, the magnetic flux in one state can tunnel into the other state. The MQT is reported not only in superconductors but also in ferromagnets such as a domain wall in the mesoscopic wire [31,32], the single domain particle [33] and the magnetic molecule [34].

There are some perspective of interest in the MQT. First, it is whether "the macroscopic object can tunnel or not". It is surprising that the large object behaves as a quantum particle. Second, there are effects of the surrounding environment, or the other degrees of freedom such as the electrons, photons and magnons, on the tunnel effect. These degrees of freedom interact with the degree of freedom which tunnels and these interactions work as the friction in quantum motion. We can test quantum physics with friction by studying the MQT [35]. Third, at high temperature, the macroscopic object obeys classical mechanics. If we observe that the macroscopic object recovers the quantum nature as decreasing temperature, we can perform the experiment to address the relation between quantum mechanics in the microscopic system and classical mechanics in the macroscopic system. The MQT in ferromagnets attracts the interest mainly due to the tunnel effect in the macroscopic system itself.

1.2   Current noise [36]

In this thesis, we especially focus on the current noise to probe the properties of the MTJ and here we would like to introduce the current noise. When a bias voltage is applied to a sample, the current is determined usually by Ohm's law. However, actually, the current fluctuates with time as schematically shown in Fig 1.9(a). We evaluate the current noise $(\delta I)^2$ by using current noise spectral density S_I. S_I is obtained through the fast Fourier transform of time-dependent current as follows,

$$S_I(f) = \int_{-\infty}^{\infty} e^{2\pi ft}(\delta I)^2 dt \ (\mathrm{A}^2/\mathrm{Hz}). \tag{1.13}$$

By evaluating S_I, we can obtain more information about transport dynamics which we cannot access by usual conductance measurement. Here, we introduce three types of the current noise, namely thermal noise, shot noise and $1/f$ noise.

Thermal (Johnson-Nyquist) noise

The thermal noise appears even in the equilibrium state, which originates from thermal fluctuation of electrons. The thermal noise is also called Johnson-Nyquist noise because Johnson measured it and Nyquist calculated it quantitatively in 1920s [37, 38]. The thermal noise is frequency-independent (white) noise and proportional to temperature of electron T_e, which is expressed by

$$S_{\mathrm{thermal}} = 4k_{\mathrm{B}}T_e G. \tag{1.14}$$

Here, k_{B} and G are the Boltzmann constant and the conductance of the resistor, respectively. The thermal noise can be used for the primary standard of temperature [39].

Shot noise

The shot noise occurs when current is applied to a sample. The shot noise is caused by the partition process of electrons; when electrons come into a sample, some electrons are transmitted and others are reflected. The partition process of two processes is the origin of the shot noise. The shot noise is white noise as is the thermal noise. At the zero temperature limit, the shot noise is proportional to the average of the current $\langle I \rangle$ and is given by

$$S_{\mathrm{shot}} = 2e^*\langle I \rangle F. \tag{1.15}$$

Here, e^* is the effective charge of the conducting carrier and F is called the Fano factor, which characterizes the shot noise. We can obtain the information about the effective charge and the statistical property of conducting electrons as described below.

In general, at a finite temperature, the shot noise and the thermal noise compete with

each other and the white noise at a finite voltage and temperature is calculated as

$$S_{\mathrm{I}} = 4k_{\mathrm{B}}T_eG + 2F\left[e\langle I\rangle\coth\left(\frac{eV_{\mathrm{sd}}}{2k_{\mathrm{B}}T_e}\right) - 2k_{\mathrm{B}}T_eG\right].$$ (1.16)

Here, V_{sd} is a bias voltage across the sample. This equation is plotted as a function of V_{sd} in Fig 1.10. At $V_{\mathrm{sd}} = 0$, S_I equals to the thermal noise ($4k_{\mathrm{B}}T_eG$) because there is no net current. At $e|V_{\mathrm{sd}}| \sim k_{\mathrm{B}}T_{\mathrm{e}}$, the crossover from the thermal noise to the shot noise shows a parabolic behavior. At $\mathrm{e}|V_{\mathrm{sd}}| \gg k_{\mathrm{B}}T_{\mathrm{e}}$, the shot noise is dominant and S_I is proportional to V_{sd}.

$1/f$ noise

The $1/f$ noise is usually proportional to the reciprocal of frequency and dominant in the low frequency regime and is given by

$$S_{1/f} = \frac{a}{f}.$$ (1.17)

The origin of the $1/f$ noise is considered to be electron trap in the impurity state of sample and fluctuation of the position of the scatterer [40]. Empirically, the intensity or the constant of proportionality of the $1/f$ noise a is generally proportional to the squared bias voltage V_{sd}^2. We evaluate the $1/f$ noise by using Hooge parameter α obtained from empirical Hooge's law [40]. In the tunnel junction, we can write Hooge's law as

$$S_{1/f} = \frac{\alpha V_{\mathrm{sd}}^2}{Af}.$$ (1.18)

Here, A is the junction area of the tunnel junction.

Fano factor

The Fano factor is a dimensionless parameter defined as $F = \frac{S_I}{2e\langle I\rangle}$. Taking the number of transmitting electron per time as N, $\langle I\rangle$ and $\langle(\delta I)^2\rangle$ are equal to $e\langle N\rangle$ and $e^2\langle(\delta N)^2\rangle$, respectively. Consequently, the Fano factor is derived to be $F = \frac{\langle(\delta N)^2\rangle}{\langle N\rangle}$. When there is no correlation between each transmission process (Poissonian process) or classical case, the Fano factor becomes unity because of $\langle N\rangle = \langle(\delta N)^2\rangle$. However, in case that there exist some correlations in the partition process, the Fano factor is deviated from 1. When F is less than 1, electrons are antibunching or move as if they avoid each other. On the other hand, electrons are bunching or move in a group when F is larger than unity. In this way, the Fano factor offers us a quantitative information about the statistical property of the conducting electrons.

When the conduction is described by Landauer formula explained in Sec 1.1, the Fano factor is given by [36]

$$F = \frac{\sum_{k_\parallel,j} T(k_\parallel, j)(1 - T(k_\parallel, j))}{\sum_{k_\parallel,j} T(k_\parallel, j)}.$$ (1.19)
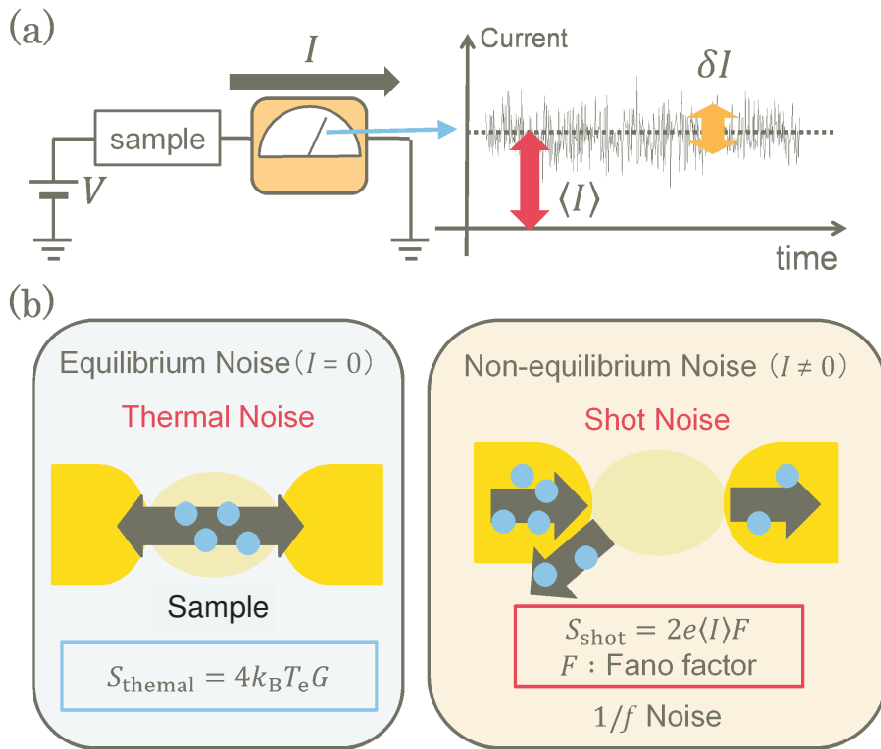
11

Figure 1.9: (a) Schematic illustration of the noise measurement. (b) Main types of the current noise which originates from conductors with schematic illustrations of the thermal noise and the shot noise.
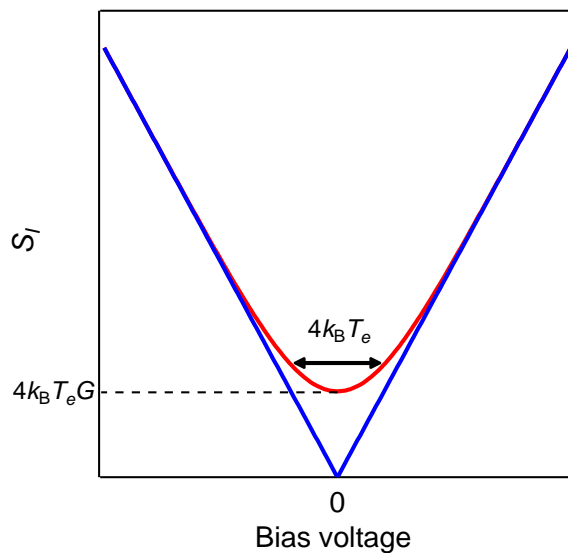

Figure 1.10: Bias voltage dependence of S_I at a finite temperature (red line) and at 0 K (blue line).

The term of $(1 - T(k_\parallel, j))$ comes from the Pauli exclusion principle. In addition to the sum of the transmission probability of conducting channels, which can be obtained by conductance measurement, we can get information about the distribution of the transmission probability for the conducting channels from the shot noise; whether electrons have similar transmission probability for all the channels or a few channels are dominant for the conduction.

Examples of the shot noise measurement

Here, we introduce several experiments of the shot noise. First, the experiments on the effective charge is described. Figure 1.11(a) shows the current dependence of the shot noise in a superconductor/normal metal junction [41]. The slope of the shot noise is twice as large as in the classical case. This result indicates that the conduction is carried not by electrons with charge e but by Cooper pairs with charge $2e$. Another experiment investigated the shot noise in the fractional quantum Hall regime [42, 43]. Although it was theoretically predicted that the effective charge e^* equals to $e/3$, it had not been confirmed experimentally. The shot noise clearly revealed that the current in the fractional quantum Hall regime was carried by the elementary charge $e/3$ as shown in Fig. 1.11(b).
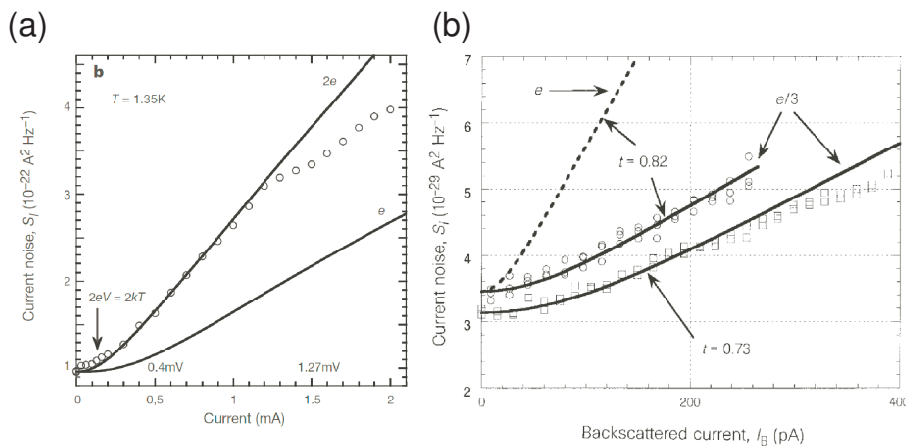
Figure 1.11: (a) Shot noise as a function of the current in a superconductor/normal metal junction [41]. Two solid curves represent the fitted line for $e^* = 2e$ and $e^* = e$, respectively. (b) Shot noise as a function of back scattering current in the fractional quantum Hall regime [42]. The solid and dotted lines represent the fitted curves for $e^* = e/3$ and $e^* = e$, respectively.

Second, the shot noise in the quantum point contact (QPC) is introduced. The QPC is a narrow constriction between two large conductors. When the width of the constriction is comparable to the Fermi wavelength, the conductance of the QPC is quantized in a

unit of $2e^2/h$. The conductance is determined by the number of conducting channels n within the construction. One channel contributes to the conductance by $2e^2/h$, which is called the quantized conductance. The QPC is a typical manifestation of Landauer formula (Eq.(1.12)) and the shot noise in the QPC is expressed by Eq.(1.19). Figure 1.12 shows the gate voltage dependence of the Fano factor in the QPC [44]. The shot noise is suppressed when the conductance equals to $\frac{2e^2}{h}n$ ($n = 1, 2, 3 \cdots$). This observation reflects that only one electron can pass through one conducting channel at the same time due to the Pauli exclusion principle.
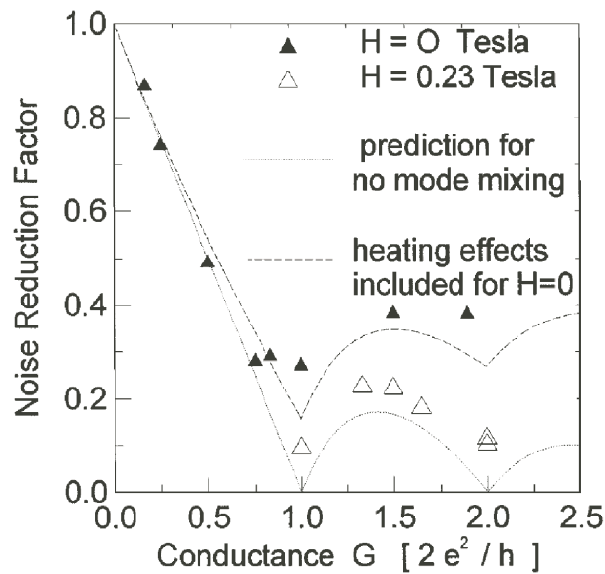

Figure 1.12: Shot noise as a function of the conductance in a quantum point contact [44]. The shot noise is suppressed when the conductance equals $2e^2/h$ and $4e^2/h$

1.3 Purpose of the study

The tunnel effect is one of the most fundamental quantum effects and plays an important role not only in pure physics but also in various applied physics researches. In this thesis, the tunnel effect in the ferromagnetic device, where the spin-dependent tunnel effect and the tunnel effect of spin degree of freedom are expected, is investigated. We focus on the magnetic tunneling junctions and the macroscopic quantum tunneling (MQT) in the magnetic vortex. Although the tunnel devices have been explored by the conventional dc measurement, the shot noise measurement is a useful tool for studying the electron transport in a tunnel junction beyond the dc measurement and enables us to clarify further the tunneling process.

In Chapter 3, the coherent tunneling in MTJs with a crystalline spinel $MgAl_2O_4$ barrier is discussed. As described above, the coherent tunneling in the MgO-MTJs is essential

for a large TMR effect, which was experimentally confirmed [24]. Recently, a similar large TMR effect is observed in the cation-site disordered spinel-based MTJs, where the cation-site disorder is considered to play an important role in the coherent tunneling [21]. However, the coherent tunneling in the spinel-based MTJs is not confirmed. In this Chapter, our purpose is to confirm the coherent tunneling in the spinel-based MTJs and to clarify whether the disordered barrier allows the coherent tunneling.

In Chapter 4, we describe the contribution of the transport processes in addition to the coherent tunneling. In MTJs, we can also consider the transport caused by the sequential tunneling intermediated by the impurity state in the barrier, in other words, the leak current due to the pinhole and the photon assisted tunneling. It is important not only for pure physics but also for applications to estimate quantitatively the contribution of these different kinds of transport process. In this Chapter, we estimate the contribution of the leak current due to the pinhole from the shot noise.

In Chapter 5, we describe the detection method of the magnetic vortex core by using microcavity fabricated on two dimensional electron gas. The magnetic vortex is a spiral magnetic structure appeared in submicrometer magnetic disk and there is a about 10 nm turned up magnetization at the center of disk, so called vortex core. The quantum tunneling of the magnetization has been discussed for a long time [75]. The magnetic vortex core is a candidate for the MQT owing to the nanoscopic size. Actually, the quantum depinning of the magnetic vortex core is reported [76]. Our motivation is to observe the MQT in the reversal of vortex core. This requires the detection of the vortex core reversal. In this Chapter, we propose the ballistic detector for the vortex core reversal and confirm whether the detector can detect or not by using billiard simulation. If we can detect it, we can proceed to test whether the magnetic vortex core reverses via the quantum tunneling.

In Chapter 6, we summarize this thesis and remark the conclusion and the future perspective.

Chapter 2

Experiments

2.1 Measurement systems

Our experimental works described in Chapters 3 and 4 were carried out in the variable temperature insert (VTI by Oxford Inc.). Samples were mounted at the top of VTI and were cooled by pumping the liquid ^{4}He. By using VTI, the temperature can be changed between 2 K and 300 K by controlling pumping speed of the liquid ^{4}He and heater. The Dewar of liquid ^{4}He has a superconducting magnet whose field can be varied from -9 T to 9 T.

2.1.1 $I - V$ measurement

To measure the resistance, the constant current measurement is performed in our study. The measurement circuit is schematically shown in Fig. 2.1. The dc current from the dc voltage/current supplier (Yokogawa 7651) mixed with small ac modulation from the lock-in amplifier (SR830) by using transformer is applied to the samples through a resistor with resistance R_C (10 or 100 kΩ) much larger than the resistance of the samples (typically 500 Ω) and the voltage signal is input to room-temperature amplifier (NF Corporation LI-75A) through the coaxial cables. The amplified signal is recorded by the digital multimeter (Keithely2000) and the lock-in amplifier. This circuit enables us to obtain the differential resistance at a certain bias voltage. The differential resistance was calibrated by high-precision resistor (MCY series, error: 0.1 %) [45].

2.1.2 Noise measurement

In the noise measurement, the current noise power spectral density S_I is converted into the voltage noise power spectral density S_V through the circuit impedance. To obtain S_V, a time-dependent voltage signal is Fourier-transformed after being amplified by the amplifier and recorded by the digitizer (NI-5922). The measured voltage noise includes not
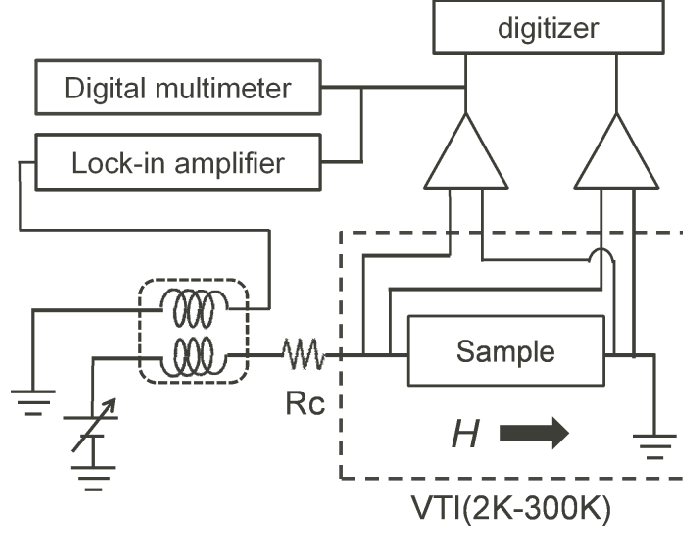
Figure 2.1: Schematic measurement circuit.

only the intrinsic noise originated from the sample but also the extrinsic noise originated from the measurement system and the surrounding environment such as the $1/f$ noise of the amplifier and external electromagnetic interferences. It is important to reduce these extrinsic noise as low as possible. To this end, in our study, the cross correlation technique is used as explained below.

Cross correlation technique in the noise [46]

As explained above, the voltage signal includes the intrinsic signal V_R and the extrinsic signal δ. In the conventional auto correlation technique, the sum of the two signals $\langle (V_R + \delta)^2 \rangle$ is obtained. On the other hand, in the cross correlation technique, two sets of the voltage signal $V_R + \delta_1^{ex}$ and $V_R + \delta_2^{ex}$, which pass different signal lines separated spatially, are measured simultaneously as shown in Fig. 2.2(b). By yielding correlation spectrum of those two signals obtained from each signal line $(V_R + \delta_1^{ex})(V_R + \delta_2^{ex})$ and by averaging it for a long time, the external noise that includes δ_1^{ex} or δ_2^{ex} vanishes because they are not correlated each other, and only the noise originated from the sample $\langle (V_R)^2 \rangle$ can be extracted.

Analysis method

A finite voltage must be applied in order to measure the shot noise because the shot noise is nonequilibrium noise. At a finite voltage, however, the $1/f$ noise and the random telegraph noise, which are dominant in low frequency, may also appear. The voltage noise power spectral density S_V measured in spinel-based MTJs is shown in Fig. 2.3. It is observed that the white noise such as the shot noise and the thermal noise cannot be
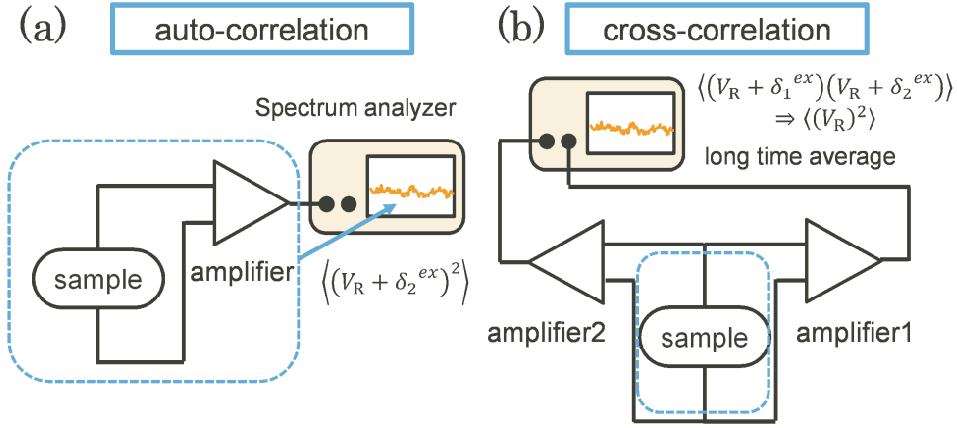
17

Figure 2.2: (a) Noise measurement by usual method. (b) Noise measurement by cross correlation method.

estimated due to the $1/f$ noise in low frequency, while the white noise is dominant in high frequency typically above 100 kHz. We can analytically extract the white noise as long as $1/f$ noise is not overwhelmingly large.

It is known that the current noise in the sample can be represented as an ac current source connected in parallel with the sample, and the measurement systems for ac current can be realized by an equivalent circuit shown in Fig. 2.4. The coaxial cables connecting the sample and the amplifier contain parallel capacitance C, and the high frequency signals are attenuated by the low-pass filter composed of the parallel capacitance and the sample resistance. Here, the followings are taken into account;

- Deviation from Ohm's law; The sample resistance is treated as the differential resistance dV/dI.

- Effect of the sample resistance to the constant current.

- The thermal noise also occurs in the resistor R_C.

The resistance and the thermal noise of R_C is a constant value independent of the bias voltage V_{sd}. Considering only the white noise and the $1/f$ noise, the voltage spectral density measured in the equivalent circuit shown in Fig. 2.4 is expressed as

$$S_V = S_V^* \frac{R^{*2}}{1 + (2\pi f C R^*)^2}, \tag{2.1}$$

$$S_V^* = G_{AC}^2 \times \left(S_{V\_white} + a\frac{1}{f} \right), \tag{2.2}$$

and

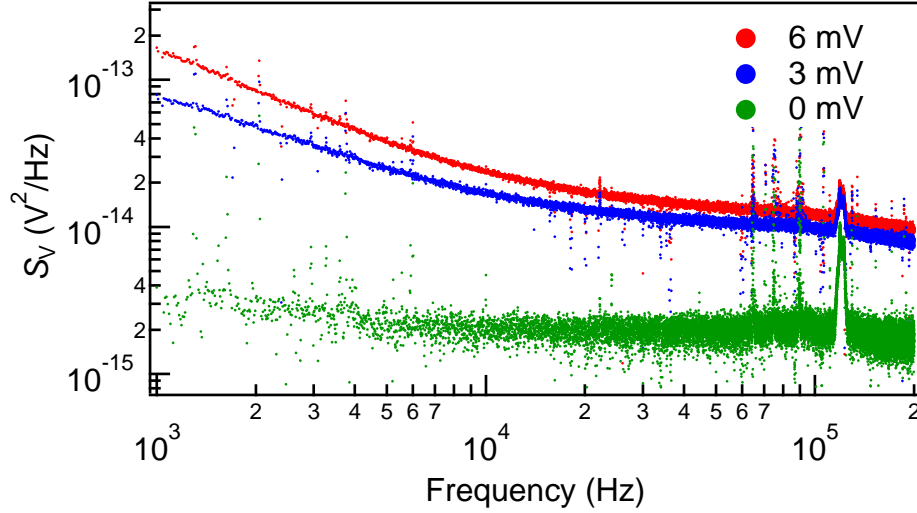$$R^* = \frac{\frac{dV}{dI}|_I R_C}{\frac{dV}{dI}|_I + R_C}. \tag{2.3}$$

18

Figure 2.3: Example of the measured voltage noise spectral density in spinel-based MTJs at $V_{\mathrm{sd}} =0$, 3, and 6 mV.

Here, G_{AC} is the gain of amplifier. First, the attenuation due to the low-pass filter is compensated by using Eq.(2.1). The value of the parallel capacitance is ~ 760 pF in our measurement system. The measured voltage noise spectral density S_V and the compensated voltage noise spectral density S_V^* is shown in Fig. 2.5. The $1/f$ contribution is almost subtracted. For the analysis of the $1/f$ noise, numerical fitting is performed to obtain a by using Eq.(2.2). We can also estimate the white noise component S_{V_white} by this method. However, it is usually not easy to determine S_{V_white} with a high precision. Therefore, the histgram analysis is necessary.

Histgram analysis

In Fig. 2.5(b), the compensated voltage noise spectral density S_V^* still contains the spike noise, which is originated from the external electromagnetic interferences. The histgram analysis has an advantage as it is less likely to be disturbed by such spike noise. We create histgram from S_V^* in the frequency domain of 140-180 kHz in the Chapter 3 and 100-140 kHz in the Chapter 4 as shown in Fig. 2.6. By comparing Figs. 2.5(b) and 2.6, it is clear that the spike noise is well discriminated from the white noise that we would like to obtain. This histgram is fitted to obtain S_{V_white} by using Gaussian function.

2.2 Fabrication

In our study of Chapter 5, we fabricated gate electrodes and a disk of permalloy (Py; $Fe_{20}Ni_{80}$) on the GaAs/AlGaAs heterojunction semiconductor (Sumitomo Electric In-
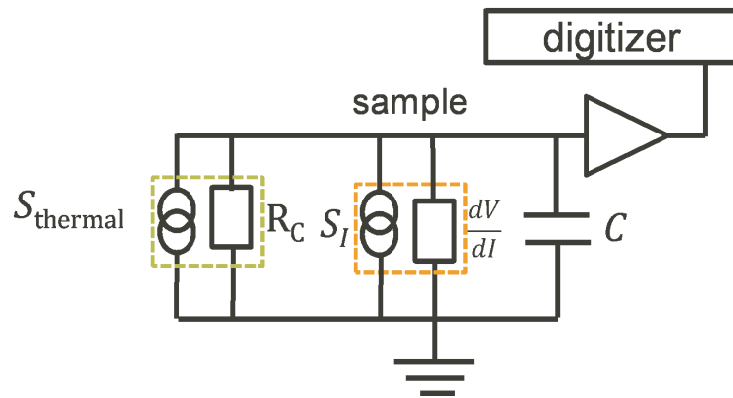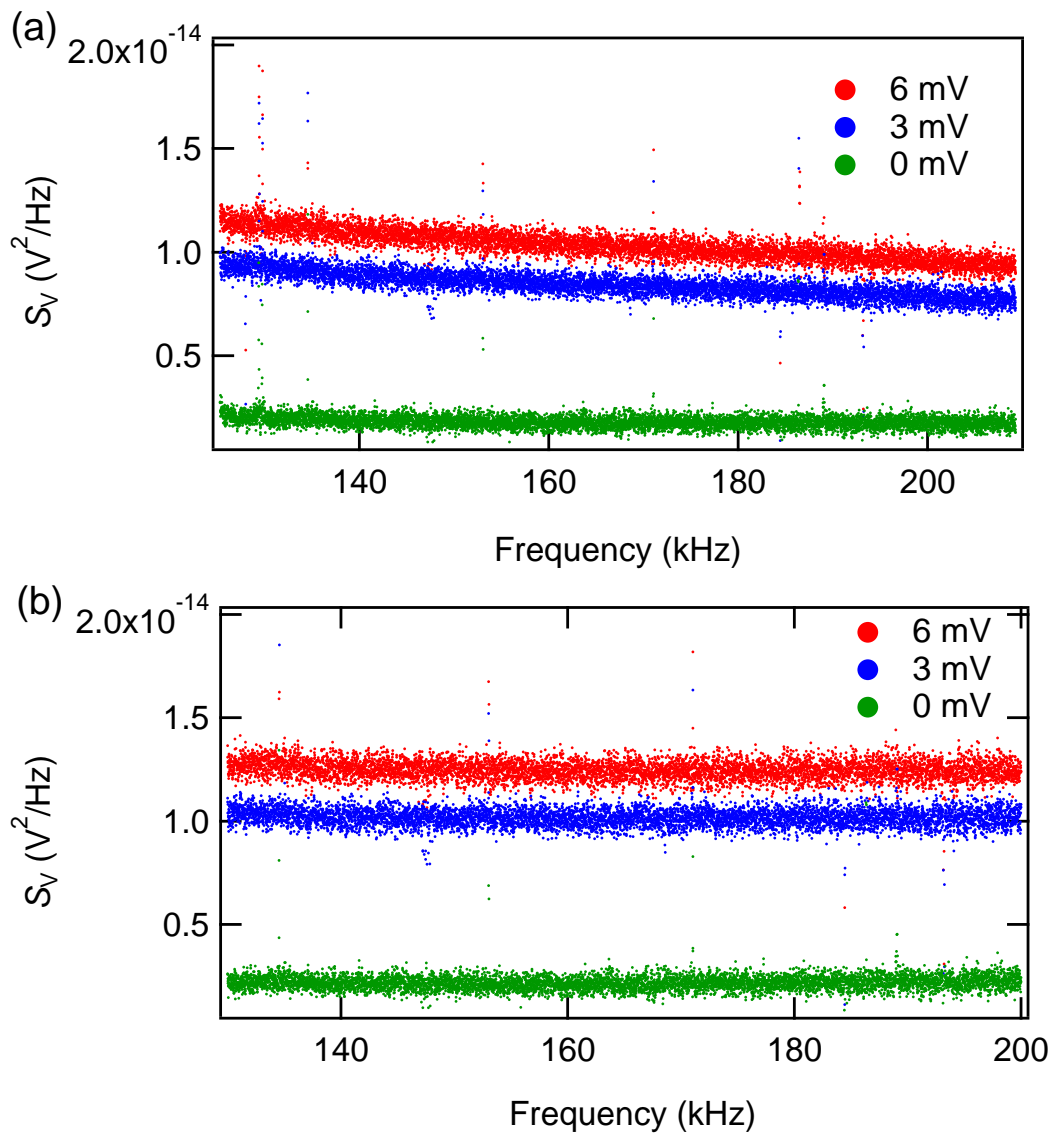
Figure 2.4: Equivalent circuit for AC current

Figure 2.5: Voltage noise spectral density (a) before compensation of lowpass filter and (b) after compensation of lowpass filter.
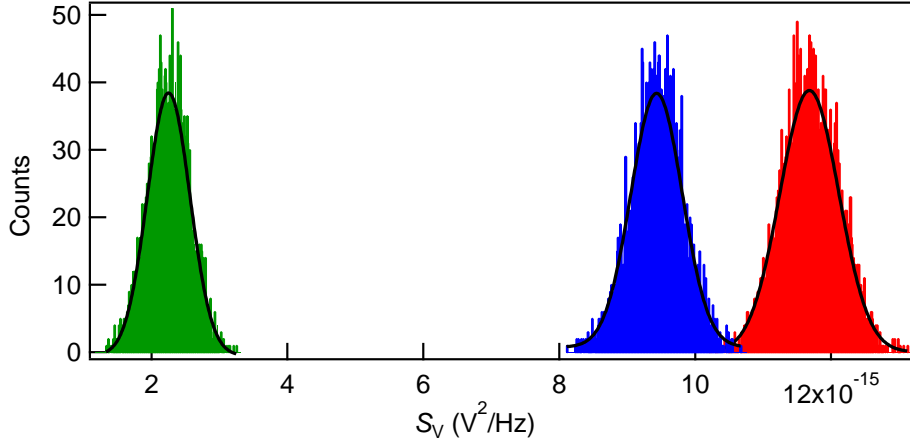
Figure 2.6: Histgram from the voltage noise spectral density in Fig. 2.5(b). The solid curves represent the fitted Gaussian function.

dustries, HEMT epitaxial wafer) formed by the molecular beam epitaxy method. This heterojunction semiconductor contains two dimensional electron gas (2DEG) as explained in Chapter 5, in the GaAs/AlGaAs heterojunction interface. The fabrication method is explained in the followings in detail.

1. Hall bar fabrication on 2DEG

   2DEG is patterned into the hall bar by photolithography and wet etching. The resist S1813G(SHIPLEY) is used for photolithography. For the wet etching. we use acid aqueous solution prepared by mixing phosphoric acid in a concentration of 85 %, hydrogen peroxide water in a concentration of 30-35.5 % and distilled water in the ratio of H_3PO_4: H_2O_2: H_2O = 1.1: 0.9: 48. In this solution, H_3PO_4 dissolve the surface of GaAs oxidized by H_2O_2.

2. Ohmic contact fabrication

   The multilayer stack of Au(20 nm)/Ge(10 nm)/ Au(20 nm)/ Ge(10 nm)/ Au(20 nm)/ Ge(10 nm)/ Au(20 nm)/ Ge(10 nm)/ Au(20 nm)/ Ge(10 nm)/ Ni(30 nm)/ substrate is pattered by photolithography and deposited by the electron beam heating type vapor deposition. The ohmic contact is formed by heating multilayer at 450 degree in vacuum and diffusing Ni and Au into GaAs.

3. Fabrication of gate electrodes and Py disk

   The Au/Ti electrode is fabricated by photolithography, EB lithography and the electron beam heating type vapor deposition. The optical microscope and scanning electron microscope images are shown in Fig. 2.7 A schottky barrier is formed between this gate electrode and GaAs. Py disk is fabricated by the same method.
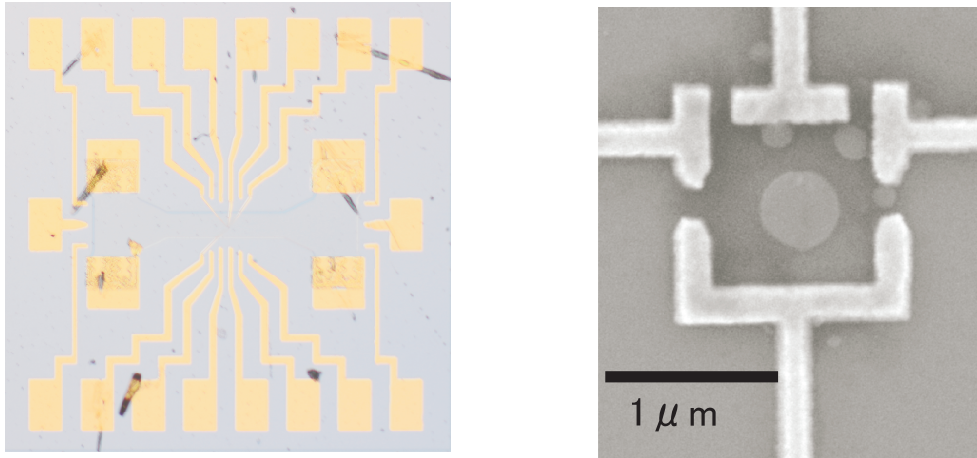
21

Figure 2.7: Optical microscope and scanning electron microscope images of our sample.

Chapter 3

Coherent tunneling in spinel-based magnetic tunneling junctions

3.1 Background

In the field of electronics, which is typified by the transistor, the charge of electrons has been utilized for the development of the devices. Recently, there arises a research field called spintronics, where the active manipulation of both the charge and the spin degrees of freedom is studied [47]. One of the essential phenomena is the spin-dependent transport in the ferromagnetic systems. The typical example is the tunneling magnetoresistance (TMR) effect in magnetic tunnel junctions (MTJs).

3.1.1 Spinel-based MTJs

In Chapter 1, the TMR effect in MTJs is described. In MTJs with a amorphous Al_2O_3 barrier, the MR ratio is at most 100 %. On the other hand, in MgO-based MTJs, a very large MR ratio is observed [15, 16]. It was discussed that the coherent tunneling of the highly spin-polarized electrons in the Δ_1 Bloch state is considered to be essential for the prominent TMR effect in the MgO-based MTJs. MgO-based MTJs have been used in hard disk drive read heads and is one of the main topics in the spintronics field. However, the lattice mismatch between MgO and Fe is not small (about 3 %) and the misfit dislocations are induced. More recently, a similar large TMR ratio was obtained in the MTJs with a crystalline spinel ($MgAl_2O_4$) barrier [20, 21], whose structure is shown in Fig. 3.1(a). The MTJs with a spinel barrier have two advantages, that is, its nondeliquescence, which mean that the spinel barrier would be more stable than MgO barrier, and its small lattice mismatch (less than 1% for an Fe electrode) compared with that of the MgO barrier case, which leads to the less misfit dislocations.

The theoretical study predicted that there exists the coherent tunneling of the Δ_1 state
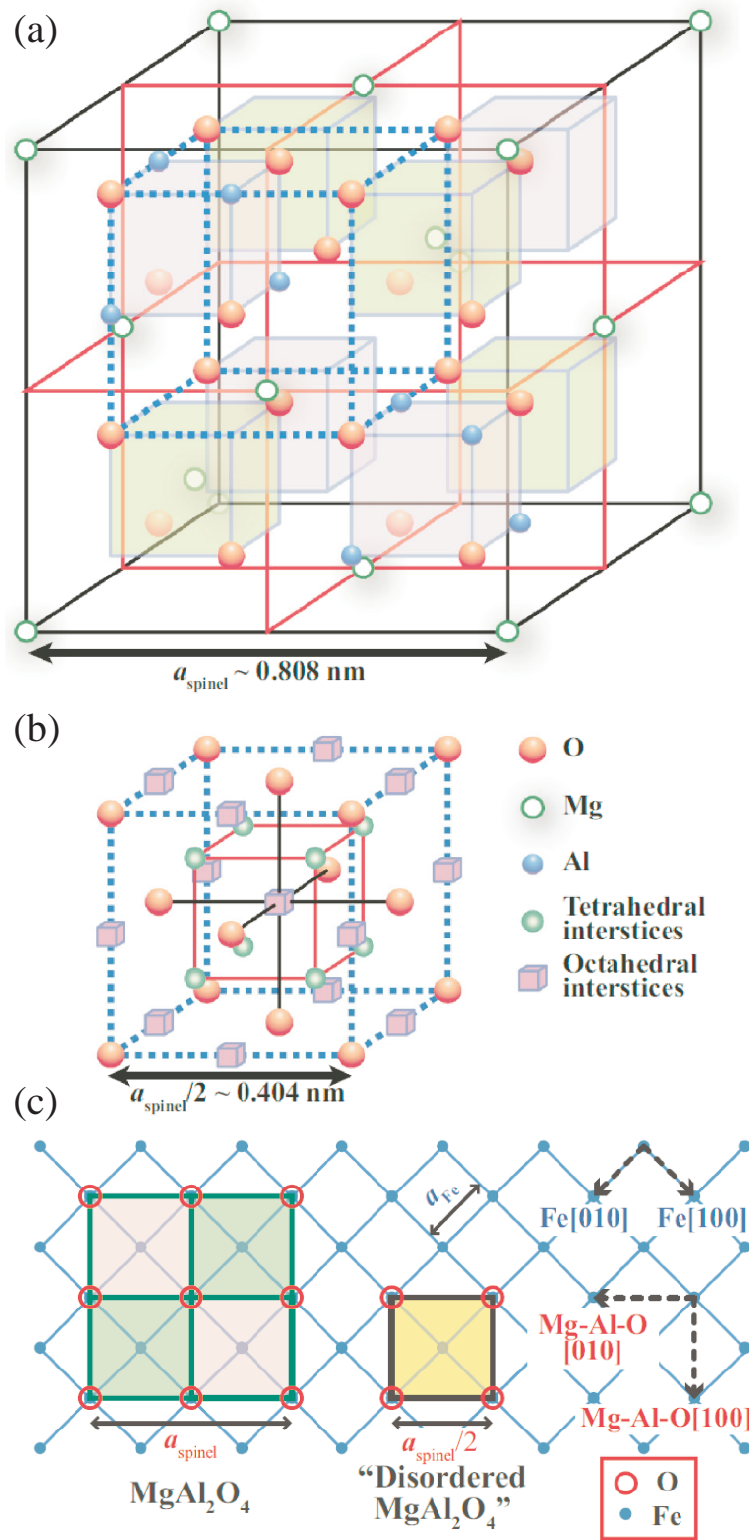
Figure 3.1: Schematic illustration of (a) normal spinel $MgAl_2O_4$ structure and (b) spinel structure with cation-site disorder. (c) Relationships between $MgAl_2O_4$ and Fe layers at the interface [21].

in $MgAl_2O_4$-based MTJs as well as in MgO-based MTJs [64]. However, the nature of the coherent tunneling in the spinel-based MTJs could be different from the case in MgO-based MTJs. The lattice constant of $MgAl_2O_4$ is twice as large as that of bcc Fe as shown in Fig. 3.1(c) and therefore a band-folding effect in the two-dimensional Brillouin zone of the in-plane wave vector occurs because the lattice constant of Fe at the interface of the $MgAl_2O_4$ layer becomes twice as large. Due to this band-folding effect, the Δ_1 electrons with the minority spin contribute to the conductance, which suppresses the TMR effect. In order to prevent the band-folding effect, cation-site disorder, which makes the effective lattice constant of the barrier reduced to half as shown in Figs. 3.1(b) and 3.1(c), is induced by performing the oxidation and postannealing processes at temperatures much lower than the melting point of $MgAl_2O_4$ (2122 ℃). This cation-site disorder enhances the TMR effect in the spinel-based MTJs [21]. It is of primary importance to experimentally investigate whether the coherent tunneling occurs in such a cation-site disorder spinel barrier as well as in the MgO-based MTJs.

3.1.2 Shot noise in MgO-based MTJs

In order to consider the shot noise in $MgAl_2O_4$-based MTJs, the shot noise in MgO-based MTJs is briefly explained. It is mentioned that the Fano factor in a tunnel junction is given by Eq.(1.19). Taking the spin degree of freedom into account, the Fano factor in MTJs is given by

$$F = \frac{\sum_{k_\parallel, j, \sigma} T_{\mathrm{P(AP)}}(k_\parallel, j, \sigma)(1 - T_{\mathrm{P(AP)}}(k_\parallel, j, \sigma))}{\sum T_{\mathrm{P(AP)}}(k_\parallel, j, \sigma)}. \tag{3.1}$$

Here, $k_\parallel$ is the wave number parallel to the tunnel barrier, j represents the Bloch state of electrons and σ is the electron spin. In normal metal/insulator/normal metal junctions, the Fano factor is unity (Poissonian process), because the tunnel probability in the tunnel junction is usually much smaller than 1 ($T \approx 0$). In MTJs, the situation would be the same as normal tunnel junction when the tunnel probability is much smaller than 1. However, what was observed in MTJs was more complicated than this simple expectation as we will see below.

In MgO-based MTJs, the Poissonian shot noise was observed [50–52]. Later, the shot noise in MgO-based MTJs with a thin barrier was reported [24]. Figure 3.2 shows the noise power spectral density S_I as a function of the bias voltage. The solid and dotted curves represent the fitted curve and the curve corresponding to $F = 1$, respectively. F for the parallel (P) configuration is clearly reduced from unity, while F for the anti-parallel configuration is close to 1. This result was proven to be quantitatively consistent with theoretical calculation by the first principle [53], supporting the relevance of the coherent tunneling model in the MgO barrier as discussed below.
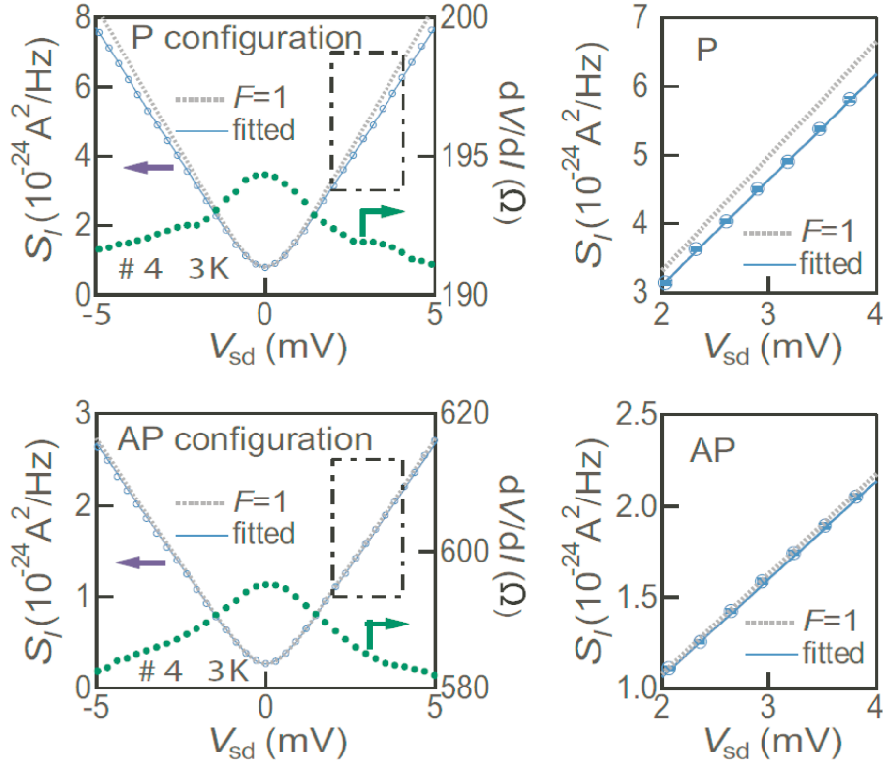
Figure 3.2: Shot noise in the MgO-based MTJs with a thin barrier. The shot noise is suppressed in the P configuration [24].
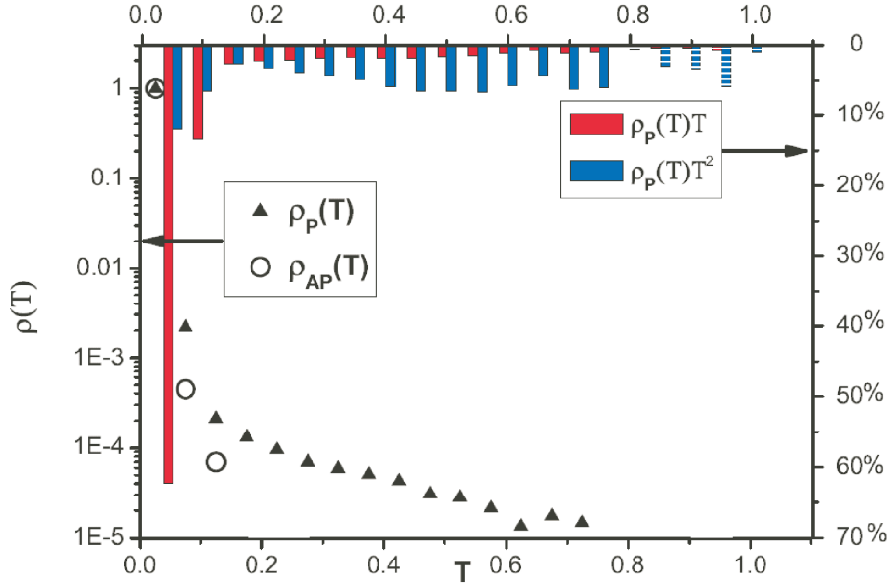

Figure 3.3: Distribution of the tunneling probability in MgO-based MTJs calculated by first principle [53].

Actually, the Fano factor in MTJs is expressed by expanding Eq.(3.1);

$$
\begin{aligned}
F &= \frac{\int \rho(T)T(1-T)dT}{\int \rho(T)TdT} \\
&= 1 - \frac{\int \rho(T)T^2dT}{\int \rho(T)TdT}.
\end{aligned}
\tag{3.2}
$$

Here, $\rho(T)$ is a distribution function of the tunneling probability T. In the case of thick barrier, $F \simeq 1$ for both configurations because the tunneling probability decreases exponentially with increasing barrier thickness, and T of all the electrons are almost 0. On the other hand, in the case of thin barrier, $\int \rho(T)T^2dT$ for the P configuration has a finite value due to the peak of tunneling probability around $k_\parallel = 0$ for Δ_1 coherent tunneling, which suppresses F. In the AP configuration, Δ_1 electron does not contribute to the conductance and the Fano factor is almost unity.

Figure 3.3 shows the detail of the distribution function of T in the disordered Fe/MgO/Fe tunnel junction [53]. $\rho(T)$ and the contribution of T and T^2 ($\rho(T)T$ and $\rho(T)T^2$) are shown in the left and right axis, respectively. For the AP configuration, $\rho(T)$ rapidly decreases with increasing T. In contrast, for the P configuration, $\rho(T)$ has a finite value even when T is larger than 0.5. For example, at $T = 0.5$, $\rho(T)$ is about 3×10^{-5}. Although it is very small, it has a large contribution to $\rho(T)T^2$ and to suppression of the Fano factor. Thus, the observed sub-Poissonian shot noise in MgO-based MTJs gives the evidence for coherent tunneling in the MgO barrier. Although the coherent transport via the Δ_1 states has been inferred theoretically and experimentally, a convincing experimental signature can be obtained through the shot noise measurement.

Our purpose of this study is to examine whether this observation is also obtained in the spinel-based MTJs.

3.2   Sample

The samples measured in this study are the Fe/MgAl$_2$O$_4$/Fe based MTJs with two different barrier thickness shown in Fig. 3.4(a) fabricated by Seiji Mitani, Hiroaki Sukegawa and Shinya Kasai in National Institute for Materials Science [20, 21]. The thickness of thin insulating layer MgAl$_2$O$_4$ is 1.5 nm, which is fabricated by the oxidation of Mg(0.45)/Mg$_{33}$Al$_{67}$(0.9) (thickness in nm). Other device with thick insulating layer is fabricated by the oxidation of Mg(0.45)/Mg$_{19}$Al$_{81}$(1.4) (the exact thickness was not directly measured). The junction area (JA) are 1.5×0.5, 3×1, and 6×2 μm^2 for MTJs with a thin barrier and 8×4, 10×5, and 12×6 μm^2 for MTJs with a thick barrier. Resistance-Area (RA) products ($R_{\mathrm{P}} \times$ junction area) are about 140 $\Omega \cdot \mu$m^2 and 5.7 k$\Omega \cdot \mu$m^2, respectively.

Figure 3.4(b) shows the typical MR curve of sample No.2 at 4K. The MR ratio is 280 %. In these MTJs, one ferromagnetic layer (pin layer) has a higher coercive force than the other one (free layer) because of the antiferromagnetic coupling between the pin layer and the antiferromagnetic layer. The smaller MR curve was caused as the free layer reversed on the way of reversal of the pin layer. The characteristics of the nine MTJs that we used in this study (No. 1 - 9) are summarized in tables 3.1 and 3.2. The MR ratio of sample No.1 is smaller than the other samples due to the incomplete AP configuration. The magnetic structure of Fe in sample No.1 might be multidomain.

Sample number	JA(μm^2)	MR ratio(%)
No.1	1.5×0.5	190
No.2	1.5×0.5	280
No.3	3×1	281
No.4	3×1	288
No.5	6×2	297
No.6	6×2	301

Table 3.1: Characteristics of MTJs with the 1.5 nm-thick barrier at 4 K.

Sample number	JA(μm^2)	MR ratio(%)
No.7	8×4	269
No.8	10×5	277
No.9	12×6	283

Table 3.2: Characteristics of MTJs with the thick barrier at 2 K.

3.2.1 Fabrication method of sample

In this section, the fabrication method of MTJs is explained [20, 21].

1. The MTJs studied in this work consist of the multilayer stack of Cr(40)/Fe(30)/ Mg(0.45)/Mg$_{33}$Al$_{67}$(0.9)O$_x$ or Mg$_{19}$Al$_{81}$(1.4)O$_x$/Fe(7)/IrMn(12)/Ru(7 or 4) grown by magnetron sputtering on MgO(001) substrate. The (Mg/Mg-Al)-O$_x$ barrier layer was fabricated by plasma oxidation in an Ar+O$_2$ atmosphere.

(a)

Ru(7 nm) Cap layer

IrMn(12 nm) AF layer

Fe(7 nm) Pin layer

$MgAl_2O_x$(1.5 nm) Insulating layer

Fe(30 nm) or Free layer

Cr(40 nm)

Mg(001) Sub
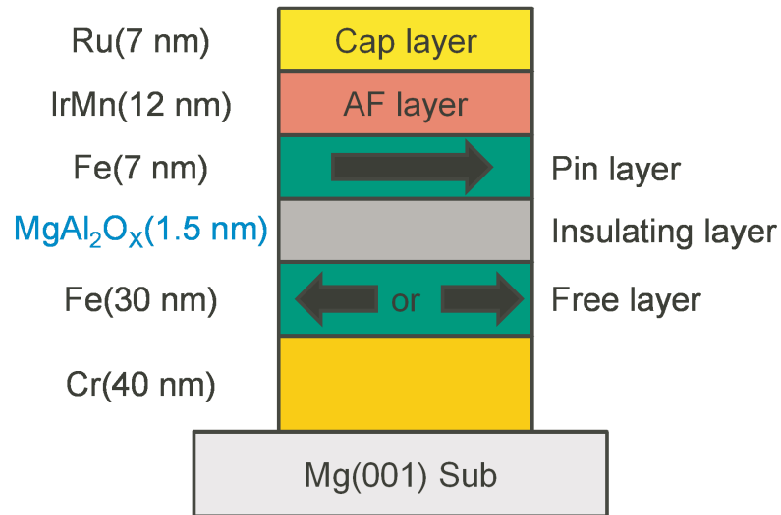
(b)

Figure 3.4: (a) The structure of MTJs. (b) Typical MR curve of sample No.2 at 4 K.

2. The multilayer was patterned into 1.5×0.5, 3×1, 6×2 8×4, 10×5 and 12×6 μm^2 by photolithography and Ar milling and Au/Ti electrodes are fabricated.

3. MTJs were annealed at 175 °C for 15 min under a magnetic field of 5 kOe.

In this MTJs, the pin layer is Fe(7). At the interface between Fe(7) layer and IrMn (antiferromagnet) layer, localized spins of two layers are in the AP configuration due to the exchange coupling (antiferromagnetic coupling). The pin layer is strongly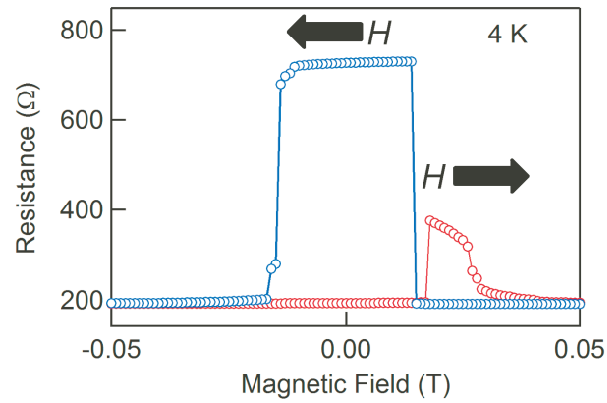 pinned by the antiferromagnetic coupling with IrMn layer, because IrMn layer is hardly affected by the external magnetic field. The difference between the coercive forces of the pin layer and free layer leads to achieve the P and AP configurations in the zero magnetic field. The annealing was performed to align the magnetizing direction.

3.3 Experimental results and Discussion

3.3.1 Shot noise

The measurements were carried out in the variable temperature insert (Oxford Inc.) at 4 K for MTJs with a thick barrier and 2 K for MTJs with a thin barrier, respectively. Figure 3.5(a) shows the voltage noise power spectral density of sample No.2 for the P configuration. We can obtain the clear white noise. In order to estimate S_V, the histgram analysis was performed as explained in Chapter 2. The histgrams and fitted Gaussian function for the data presented in Fig. 3.5(a) are shown in Fig. 3.5(b). S_V was converted to S_I by the expression

$$S_I = \frac{S_V}{(\frac{dV}{dI})^2}.$$ (3.3)

Figures 3.6(a) and 3.6(c) show the experimental result of the differential resistance dV/dI and the S_I of No.2 for the P and AP configurations as a function of the bias voltage (V_{sd}) at 4K. The differential resistance in both configurations show the asymmetric zero bias anomaly, which is consistent with the previous report for this type of MTJs [20]. It may indicate the difference in microstructure between the top and bottom electrodes due to the insertion of Mg layer. At $V_{\text{sd}} = 0$, S_I is equal to the thermal noise $4k_{\text{B}}T(1/R^*)$ with T = 4 K. Here, $R^* = (dV/dI)R_{\text{C}}/((dV/dI) + R_{\text{C}})$ as described in Chapter 2. The obtained S_I is symmetric with regard to the bias voltage reversal. The parabolic behavior at finite bias($|eV_{\text{sd}}| \sim k_{\text{B}}T$) indicates the crossover from the thermal noise to shot noise, and S_I is linearly dependent on V_{sd} for $|eV_{\text{sd}}| \gg k_{\text{B}}T$. All these features agree with those expected from the conventional shot noise theory as explained in Chapter 1.

In order to determine F, the numerical fitting was performed by using the following equation:

$$S_I = \frac{4k_{\text{B}}T}{R^*} + 2\left[eI\coth\left(\frac{eV_{\text{sd}}}{2k_{\text{B}}T_{\text{e}}}\right) - \frac{2k_{\text{B}}T}{R^*}\right].$$ (3.4)
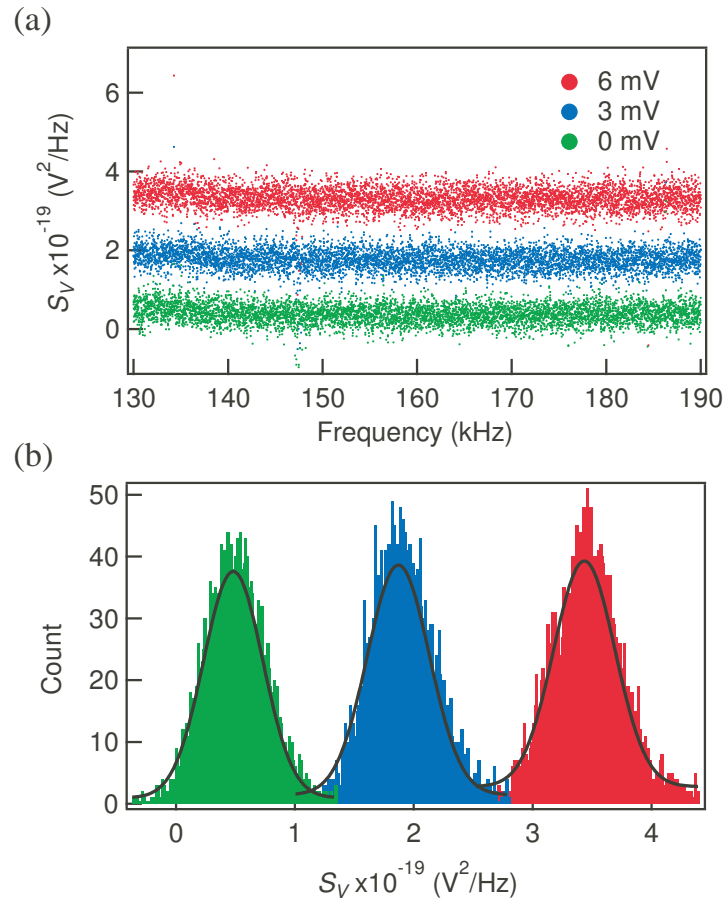
Figure 3.5: (a) Measured voltage noise power spectral density at 0, 3, and 6 mV. (b) Histgram from the voltage noise spectral density in Fig. 3.5(a). The solid curves are fitted Gaussian function.

The numerical fitting was performed by using the nonlinear lease-square regression analysis taking the experimental errors into account. The results of numerical fitting are superposed in Figs. 3.6(a) and 3.6(c) for the P and AP configurations, respectively. The solid and dashed curves represent the fitted curve and the Poissonian case ($F = 1$), respectively. Figures 3.6(b) and 3.6(d) show the corresponding expanded view of Figs. 3.6(a) and 3.6(c). As seen in Fig. 3.6(b), F for the P configuration (F_{P}) is reduced from unity to be $F_{\mathrm{P}} = 0.979 \pm 0.009$, where the error bars indicate 99.73 % confidential interval. In contrast, F for the AP configuration (F_{AP}) is very close to 1 ($F_{\mathrm{AP}} = 1.002 \pm 0.010$).

Figure 3.7(a) shows the junction area dependence of the Fano factor in MTJs with the thin barrier and the Fano factor of all the samples is compiled in Tables 3.3 and 3.4. In MTJs with the thin barrier, F_{P} is less than 1, while F_{AP} statistically equals to 1.00 expept for sample No.1. It is noted that in sample No.1 for the AP configuration, the $1/f$ noise contribution is much larger than other samples, and the estimated Fano factor ranges between 1.01 and 1.05 depending on the frequency range for the histgram analysis. In the P configuration, however, the $1/f$ noise is confirmed to have no influence on the F_{P} value. It is the most important observation that for the both configurations, the Fano factor does not depend on the junction area. This result indicates that the reduction of F is not extrinsic affect such as the impurity state. The Fano factor in MTJs with the thick barrier is compiled in Table 3.4 shown in Fig. 3.7(b). F does not depend on the junction area and is very close to 1 for both configurations.

3.3.2   Coherent tunneling

Here we would like to discuss what we can learn from the above observation. Previously, the full shot noise in MgO-based MTJs with a 1.5 nm-thick barrier was reported [50]. Later, spin-dependent suppression of the Fano factor (typically 0.91 in the P configuration and 0.99 in the AP configuration) in MgO-based MTJs with a barrier as thin as 1.05 nm was observed [24]. These results are in agreement with theoretical study, where the shot noise in disordered Fe/MgO/Fe tunnel junctions was calculated from first principles [53], which gives the evidence for coherent tunneling in the MgO barrier. As described above, F_{P} is reduced due to the high tunnel probability of Δ_1 coherent tunneling around $k_{\parallel} = 0$. In contrast, F_{AP} is close to unity because of the absence of the Δ_1 electron.

The present result of the shot noise qualitatively agrees with the result of MgO-based MTJs. This strongly suggests that the above story is also applicable even in the cation-disordered spinel barrier, as the relevance of the coherent tunneling of Δ_1 states in the spinel-based MTJs was discussed theoretically [64]. Although the coherent tunneling in spinel-based MTJs with a thick barrier is not proved by the shot noise measurement, the coherent tunneling is expected in MTJs with a thick barrier from the fact that the MR ratio of MTJs with a thick barrier is as large as that of MTJs with a thin barrier. It should
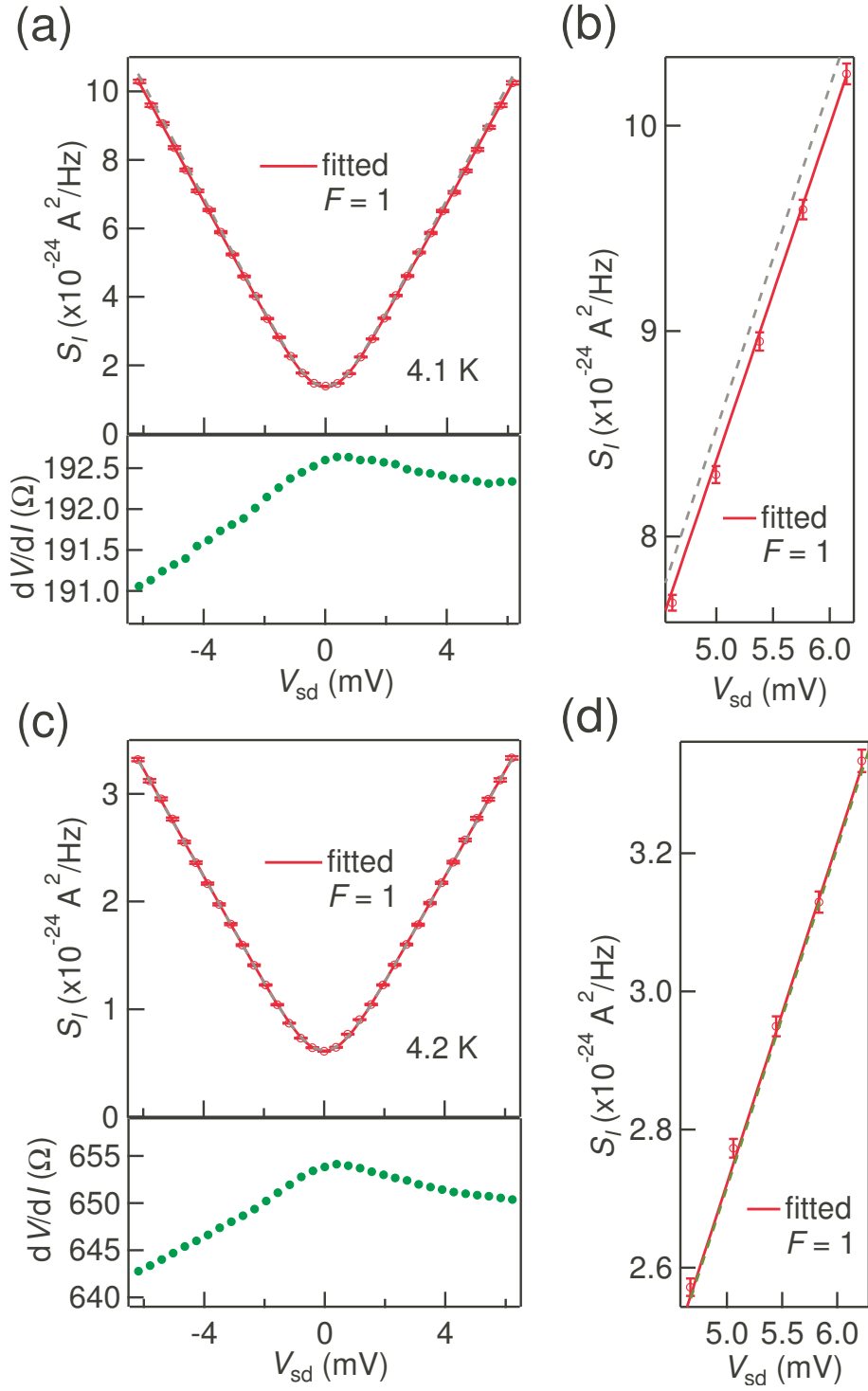
Figure 3.6: (a) Differential resistance (green circle) and current noise power spectral density (red circle) of sample No.2 for the parallel configuration. The solid curve is the fitted curve with $F = 0.979$ and the dashed curve represents the curve corresponding to $F = 1$. (b) Part of Fig. 2(a) is zoomed. (c) and (d) Counterpart of Figs. 3.6(a) and 3.6(c) for the AP configuration, respectively.

Figure 3.7: Junction area dependence of the Fano factor in MTJs (a) with the thin (1.5 nm) barrier and (b) with the thick barrier. The red and blue markers represent the P and AP configurations, respectively.

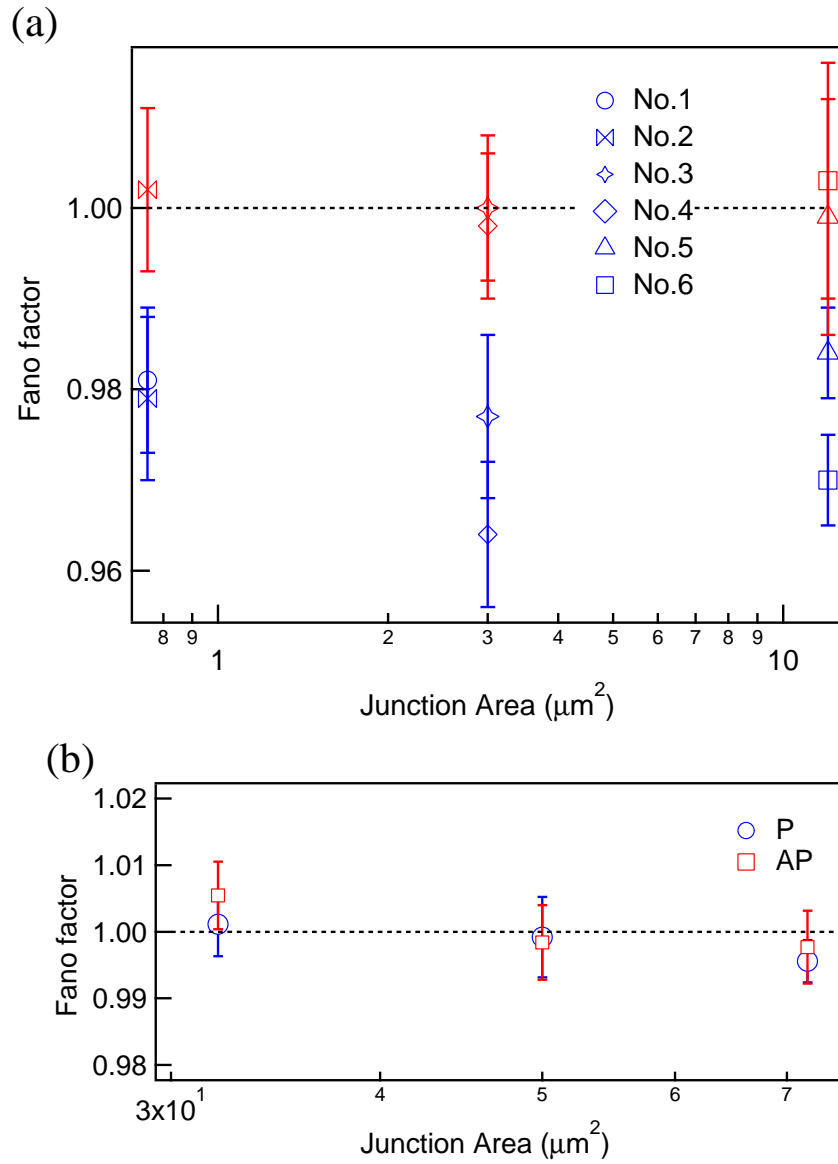| Sample No.	JA(μm^2)	Fano factor	Hooge parameter(μm^2)
No.1(P)		0.981 ± 0.008	1.3×10^{-12}
	1.5×0.5		
No.1(AP)		1.01-1.05	2.5×10^{-10}
No.2(P)		0.979 ± 0.009	1×10^{-12}
	1.5×0.5		
No.2(AP)		1.002 ± 0.009	2.5×10^{-11}
No.3(P)		0.977 ± 0.009	2.0×10^{-12}
	3×1		
No.3(AP)		1.000 ± 0.008	9.0×10^{-11}
No.4(P)		0.964 ± 0.008	2.6×10^{-12}
	3×1		
No.4(AP)		0.998 ± 0.008	7.6×10^{-11}
No.5(P)		0.970 ± 0.005	5.2×10^{-12}
	6×2		
No.5(AP)		1.003 ± 0.013	6.2×10^{-11}
No.6(P)		0.984 ± 0.005	3.8×10^{-12}
	6×2		
No.6(AP)		0.999 ± 0.013	8.6×10^{-11}

Table 3.3: Fano factor and Hooge parameter of the spinel-based MTJs with a 1.5 nm-thick barrier studied in this work.

Sample No.	JA(μm^2)	Fano factor
No.7(P)		1.001 ± 0.005
	8×4	
No.7(AP)		1.005 ± 0.005
No.8(P)		0.999 ± 0.006
	10×5	
No.8(AP)		0.998 ± 0.006
No.9(P)		0.996 ± 0.005
	12×6	
No.9(AP)		0.996 ± 0.006

Table 3.4: Fano factor of the spinel-based MTJs with a thick barrier studied in this work.
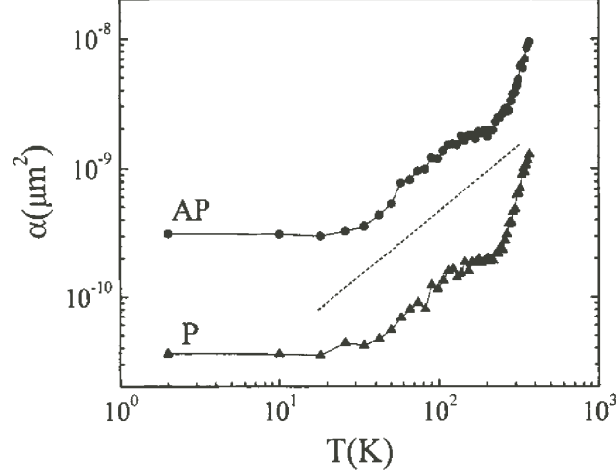
Figure 3.8: (a) Temperature dependence of the Hooge parameter of the Al_2O_3-based MTJs for P and AP configurations [48].

be also noted that the barrier thickness of the present MTJs with $F_P \sim 0.98$ is as thick as 1.5 nm, where the Poissonian shot noise would be the case theoretically for MgO-based MTJs. We do not understand the exact reason why the suppression of F_P is observed for a thick case, while it may have a relation with that RA product of the present MTJs (140 $\Omega \cdot \mu m^2$) is smaller than that of the MgO-based MTJs with a 1.5 nm-thick barrier (500 $\Omega \cdot \mu m^2$ to 50 $k\Omega \cdot \mu m^2$) [50]. As a remarks, the experimental observation that $F_{AP} > F_P$ with F_{AP} significantly suppressed below 1 was reported for amorphous Al_2O_3-based MTJs, which was attributed to the tunneling mediated by localized impurity states inside the barrier [49]. However, the present result of $F_{AP} > F_P$ with F_{AP} very close to 1 is not likely to be explained within this model, where F is suppressed for both configurations.

In addition to the shot noise measurement, the coherent tunneling is proved by other methods. In MgO-based MTJs, where the barrier thickness of MgO t_{MgO} changes continuously in the single substrate owing to the wedge shaped MgO barrier, the MR ratio oscillates with t_{MgO} [23]. It is considered to originate from the interference of the electron and to be the evidence of the coherent tunneling. In this study, however, we can directly observe the conducting electrons, and the present result would be the most direct proof of the coherent tunneling. Moreover, the Fano factor characterizes the distribution of the tunneling probability, and it is indicated that in MTJs with a thin barrier, there exist electrons with the tunneling probability larger than 2 % based on the theoretical results shown in Fig. 1.8 [9].

3.3.3 $1/f$ noise

Finally, we discuss $1/f$ noise in our MTJs. First, we briefly describe what the 1/f noise indicates. In the case of applications such as the read head of magnetic recording medium and magnetic sensor, the electrical signals of MTJs are measured. There, the electrical noises, especially the $1/f$ noise disturb the detection of the electrical signals. For these applications, the reduction of the $1/f$ noise is very important and many studies have been carried out [45, 48, 54–63]. Amplitude of the $1/f$ noise is evaluated by the Hooge parameter α given by

$$S_{V,1/f} = \frac{a}{f} \tag{3.5}$$

and

$$a = \frac{\alpha A}{V^2} \tag{3.6}$$

as explained in Chapter 1. Figure 3.8 shows the temperature dependence of α of Al_2O_3-based MTJs. The followings are known about the $1/f$ noise in MTJs.

- Amplitude of the $1/f$ noise for the AP configuration is usually much larger than that for the P configuration.

- α increases as the temperature increases.

The origin of the $1/f$ noise is considered to be the thermal fluctuation of magnetization, which is notable for the AP configuration.

Figures 3.9(a) and 3.9(b) show the voltage noise power spectral density of sample No.1 for the P and AP configurations, respectively. The $1/f$ noise is clearly larger for the AP configuration than for the P configuration. The $1/f$ noise observed at $V_{sd} = 0$ (mV) is the contribution of the amplifier. From the obtained spectral density between 6 and 60 kHz, we derived the a as a function of V_{sd}. The results of samples No.1 and No.2 for the AP configuration is shown in Fig. 3.9(c). As is usually case for the $1/f$ noise, the factor a shows a parabolic behavior as a function of V_{sd}. The numerical fitting is performed to obtain α by using Eq.(3.6). The Hooge parameters α are summarized in Table 3.3 and are shown in Fig. 3.10. It is noted that α of MTJs with a thick barrier is too small to be estimated because of the small α, large junction area, and small applied bias voltage. For the P configuration, α is much smaller than the AP configuration as mentioned in case of the MgO-based MTJs. For both configurations, the Hooge parameters α are roughly the same for all the MTJs, which means the uniformity of the film.

The present result, which is similar to the MgO-based MTJs, may indicate that the origin of $1/f$ noise for the P configuration is charge traps in the tunnel barrier, whereas the considerable $1/f$ noise contribution in the AP configuration suggests the magnetic origin. α of sample No.1 is much larger than other samples due to the imperfect AP

configuration which is mentioned as the origin of smaller MR ratio. The Hooge parameter of high-quality MgO-based MTJs is 3.4×10^{-13} (μm^2) at 3 K for the P configuration. Although the sample geometries are different, this value is roughly comparable to those of the present spinel-based MTJs. Such small $1/f$ noise contribution indicates the high quality of the well-crystalized spinel barrier.

3.4   Summary

In conclusion, the current noise was measured in $MgAl_2O_4$-based MTJs with two different barrier thicknesses and three different junction areas. In MTJs with a thick barrier, the Poissoinan shot noise is observed for both configurations. The Fano factor less than unity (typically 0.98) is observed for the P configuration, indicating the sub-Poissonian process of the electron tunneling, while the Poissonian shot noise is obtained for the AP configuration. These values of F do not depend on the junction area. This observation strongly suggests the relevance of the coherent tunneling in this type of MTJs. We also evaluate the $1/f$ noise by estimating the Hooge parameter α. α is larger for the AP configuration than for the P configuration, which indicates that $1/f$ noise in the AP configuration originates from the thermal fluctuation of the magnetization.
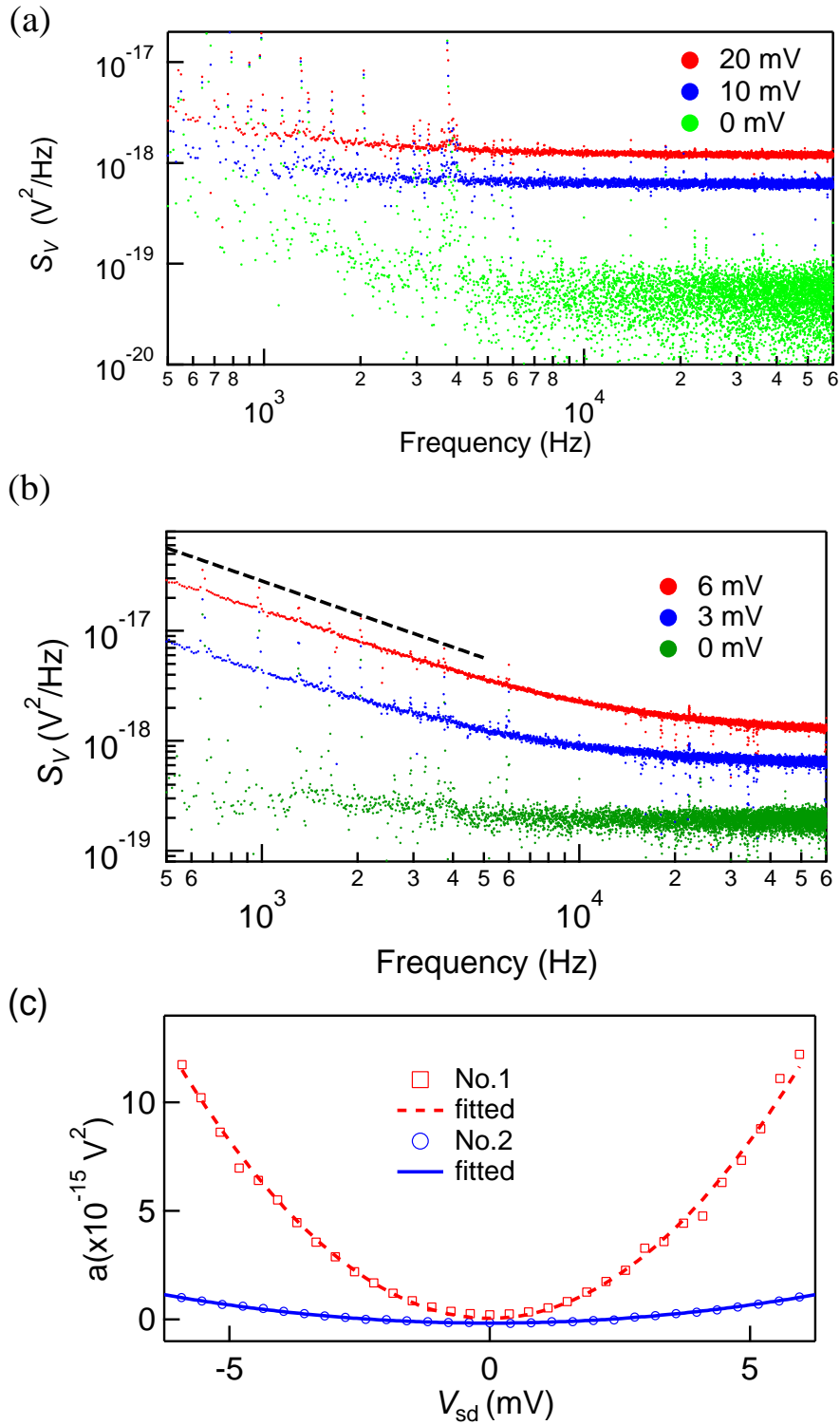
Figure 3.9: Voltage noise power spectral density of sample No.1 for (a) the P and (b) AP configuration. (b) Magnitude of $1/f$ noise of samples No.1 and No.2 for the AP configuration with a applied bias voltage at 4K.
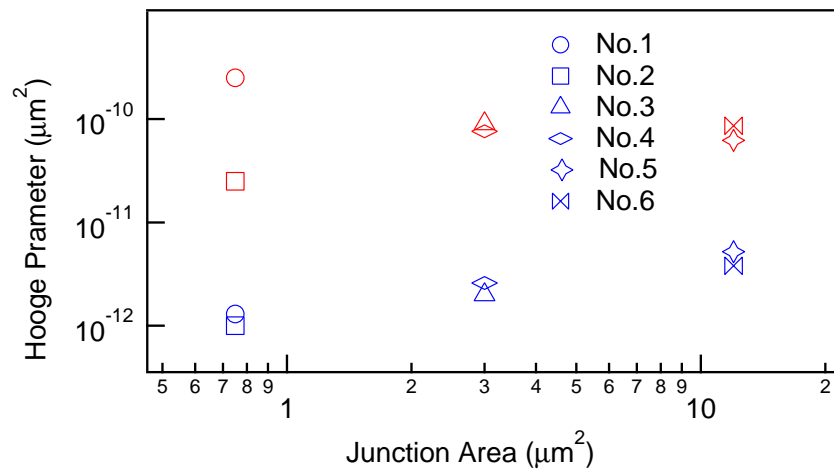
Figure 3.10: Junction area dependence of the Hooge parameter for the P (blue) and AP (red) configuration at 4 K.

Chapter 4

Microscopic tunnel processes in MgO-based magnetic tunneling Junctions

It was theoretically [53] and experimentally [24] confirmed that the electrical conduction in MgO-magnetic tunneling junctions (MTJs) is mainly carried by the coherent tunneling. However, there are also other processes such as photon-assisted tunneling [65,66], magnon-assisted tunneling [65,66], trap-assisted tunneling [67] and pinhole effect [68]. Especially when the barrier is thin, the contribution of pinholes is not negligible. In this study, we estimate the contribution of pinhole effect quantitatively by using shot noise. As we will discuss below, our achievement tells that the shot noise is useful to quantify the quality of the thin insulator in MTJs.

When the current I is applied to a tunnel junction, the shot noise occurs due to the particle nature of electron and their partition process at the junction. At zero temperature limit, the shot noise is given by $2eIF$. Here, the Fano factor F represents the degree of the deviation from the Poissonian value. In normal metal/insulator/metal junctions, the Fano factor becomes unity, which means that there is no correlation between successive electron tunneling events at the barrier, which results in the Poissonian statistics. While the above case is the most ideal one, in actual cases, F can take various values from zero to even more than unity depending on physical systems, which allows us to clarify more the electron transport via the shot noise measurement [36]. For example, it is established that the shot noise is absent ($F = 0$) in bulk resistances.

In the MTJs, the full shot noise is observed in both Al_2O_3- [48] and MgO- [24,45,50–52] based MTJs. Later, it was found that the Fano factor in the high-quality MgO-based [24] MTJs with a thin barrier is very close to 1 in the AP configuration, while it is suppressed less than unity in the P configuration. This result quantitatively agreed with theoretical calculation by the first principles [53], supporting the relevance of the coherent tunneling

model in the MgO barrier. It is, however, also possible that, depending on the quality of MTJs, the Fano factor decreases due to other transport processes such as the two step tunneling [69] and/or the electrical pinhole effect [70]. Indeed, it was reported the Fano factor in Al_2O_3-based MTJs is reduced due to the tunneling mediated by the localized state in the barrier [49].

In this Chapter, we report the shot noise study of the epitaxial Fe/MgO/Fe MTJs with various barrier thicknesses. The Fano factor is reduced from unity in the MTJs with thin barrier. We found that the factor is smaller in the AP configuration than in the P configuration unlike the previous reports [24, 53]. We explain this observation by using a simple parallel resistance model and estimate the contribution of the leak current through the junction.

4.1   Sample and measurement setup

The present MTJs consist of the multilayer stack of caplayer/IrMn(10)/Fe(10)/MgO/Fe(100)/buffer layer as shown in Fig. 4.1(a) fabricated by Shinji Yuasa, Akio Fukushima and Takayuki Nozaki in National Institute of Advanced Industrial Science and Technology [15]. The thickness of insulating layer MgO t_{MgO} changes continuously from 0.25 nm to 1.75 nm in the single substrate owing to the wedge shaped MgO barrier. This multilayer is grown by MBE on MgO(001) substrate and is patterned into MTJs structure with 200×800 and 500×2000 nm^2 by electron beam lithography and Ar ion milling. In this study, we measured 15 MTJs with various thicknesses between 1.1 nm and 1.625 nm. Figure 4.1(b) shows the MR curve of MTJs with 1.4 nm barrier at 4 K. Typically, the relative magnetization orientation switches from P configuration to AP configuration at -14 mT and from AP configuration to P configuration at -6 mT. Figures 4.2(a) and 4.2(b) show t_{MgO} dependence of resistance-area (RA) products ($R_P \times$ junction area) and MR ratios for 15 MTJs that we measured in this study. The RA product exponentially increases as a function of t_{MgO}, being a well-established behavior of a tunneling transport [71]. When t_{MgO} is very thin, the MR ratio rapidly decreases as the t_{MgO} decreases in a good agreement with the previous reports [15]. The characteristics of MTJs are summarized in Table 4.1.

The noise measurements were carried out in the variable temperature insert (VTI by Oxford Inc.) between 1.6 and 4 K. As schematically shown Fig. 4.3, the dc current with a small ac modulation is applied to the MTJ through a 100 kΩ resistor to obtain the differential resistance by means of the standard lock-in technique. The two signals of the voltage difference across the MTJs are amplified independently by using two room-temperature amplifiers (NF Corporation LI-75A) and are recorded by the two-channel digitizer (National Instruments PCI-5922). In order to reduce the external noises and

the thermal noise of the cables, the measured two sets of time domain data are cross-correlated to yield the noise power spectral density through fast Fourier transformation (FFT).

4.2   Shot noise

Figure 4.4(a) shows the typical voltage noise power spectral density S_V of MTJs with a 1.15 nm barrier for the P configuration. We performed the histogram analysis for the measured voltage noise power spectral density S_V typically between 30 kHz and 90 kHz or 90 kHz and 130 kHz as shown in Fig. 4.4(b), where the observed spectra are confirmed to be perfectly free from the $1/f$ noise of the MTJ. By carefully calibrating the measurement system and statistically treating the measurement errors, we are able to determine the Fano factor well within an accuracy of 1%. The calibration of the amplifiers, which determines the accuracy of the present noise measurement, was performed by measuring the thermal noise of several different calibrated resistances at room-temperature. In this study, we discuss the noise property obtained from 15 MTJs with various thicknesses between 1.1 nm and 1.625 nm. The resistances in series with MTJ such as the contact resistance are much smaller than the tunnel resistance and do not influence the shot noise analysis.

Figures 4.5(a) and 4.5(b) show a typical experimental result of the differential resistance (dV/dI) and the current noise power spectral density S_I for the MTJ with 1.15 nm barrier at 1.6 K as a function of V_{sd} for the P and AP configurations, respectively. S_I is deduced from S_V by using the equation $S_I = S_V/(dV_{\mathrm{sd}}/dI)^2$. At $V_{\mathrm{sd}} = 0$, S_I exactly equals to the thermal noise $4k_{\mathrm{B}}T(dV/dI)$ with $T = 1.6$ K. The obtained S_I is symmetric with regard to the bias-voltage reversal. The parabolic behavior at the finite bias ($|eV_{\mathrm{sd}}| \sim k_{\mathrm{B}}T \sim 0.14$ meV) indicates the crossover from the thermal to shot noise, and S_I linearly depends on $|V_{\mathrm{sd}}|$ for $|eV_{\mathrm{sd}}| \gg k_{\mathrm{B}}T$. All these features qualitatively agree well with those expected from the conventional shot noise theory.

To be more quantitative, the numerical fitting was performed to obtain F by using $S_I = 2e|I|F$ in the region of $|eV_{\mathrm{sd}}| \gg k_{\mathrm{B}}T$. The numerical fitting was performed for $|V_{\mathrm{sd}}| > 1$ mV for MTJs measured at 1.6 K and $|V_{\mathrm{sd}}| > 2$ mV for MTJs measured at 4 K by using the nonlinear least-square regression analysis taking the measurement errors into account. The results of the fitting are superposed in Figs. 4.5(a) and 4.5(b). The solid and dashed curves represent the fitted one and the Poissonian case ($F = 1$), respectively. As seen in Figs. 4.5(a) and 4.5(b), F is clearly reduced from unity to be 0.944 ± 0.005 for the P configuration and 0.868 ± 0.005 for the AP configuration. The same analysis was performed for the 15 MTJs. The results are summarized in Table. 4.1. One of the MTJs with 1.1 nm barrier was measured the shot noise only in the AP configuration because of
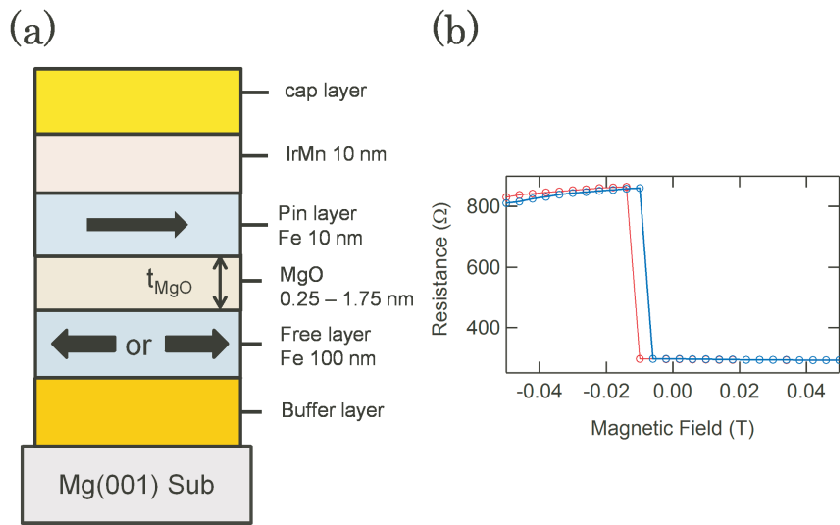
43

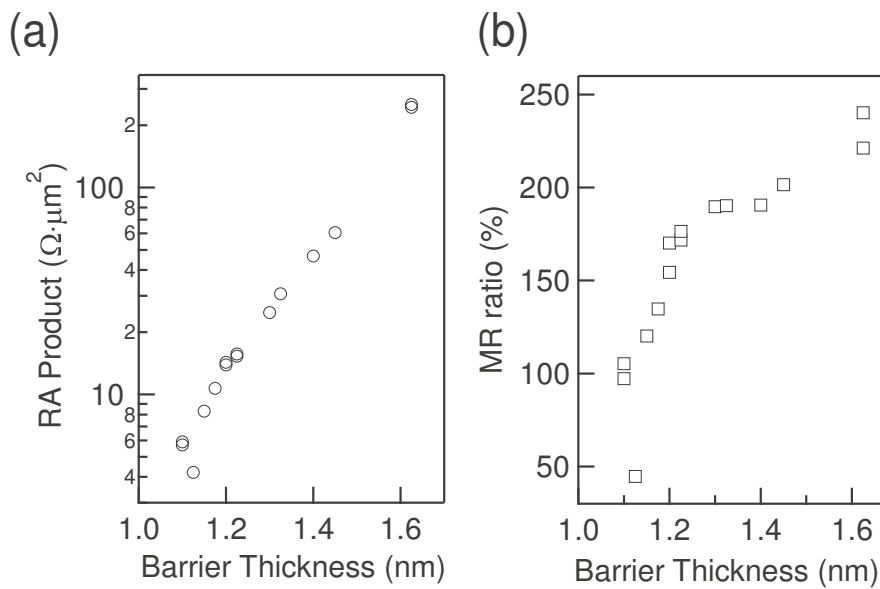Figure 4.1: (a) Structure of MTJs (b) MR curve of MTJs with a 1.4 nm barrier at 4 K.

Figure 4.2: Dependence of (a) the resistance-area (RA) products and (b) MR ratios on the MgO barrier thickness.
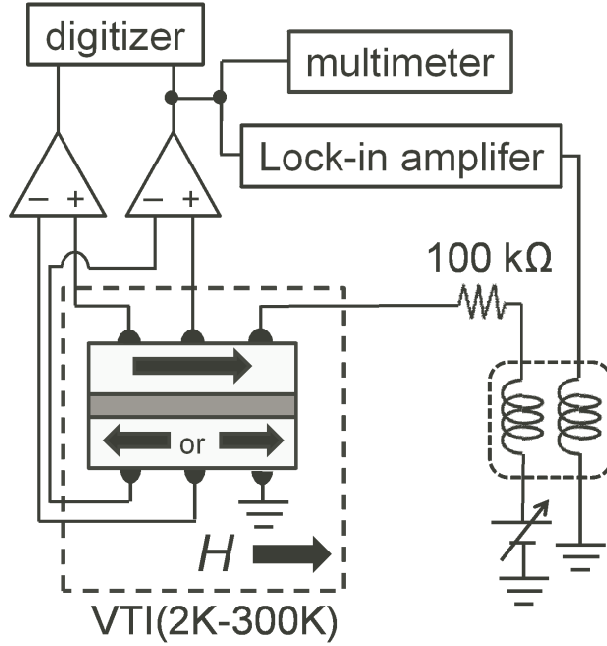
Figure 4.3: Schematic illustration of the measurement circuit.

the breakdown.

Figure 4.6 is the central experimental result of this Chapter, which shows the experimental results of the Fano factor for all the 15 MTJs with various t_{MgO} for the P and AP configurations. In the MTJs with thick MgO barrier ($t_{MgO} > 1.2$ nm), the Fano factor is very close to 1 for both configurations. On the other hand, in barriers thinner than ~ 1.2 nm, we observe the Fano factor less than one. Furthermore, the Fano factor is smaller in the AP configuration than in the P configuration. As seen in Fig. 4.6, the Fano factor varies widely from device to device, which tells that the MTJs with the same thick barrier can have different Fano factors.

4.3 Leak current model

As mentioned in Chapter 3, we obtained the full Poissonian shot noise in CoFeB/MgO/CoFeB tunnel junctions with 1.5 nm-thick barrier [50]. Later, we reported that the Fano factor is typically 0.91 in the P configuration and 0.98 in the AP configuration in the MTJs with thin barrier (1.05 nm) [24]. The result, which was reproducible for the four measured devices, quantitatively agrees with theoretical study by using first principle calculation for the disordered Fe/MgO/Fe tunnel junctions [53]. In these results, the Fano factor is smaller in the P configuration than in the AP configuration. Therefore, the present result is qualitatively different from the previous report as well as from the theoretical
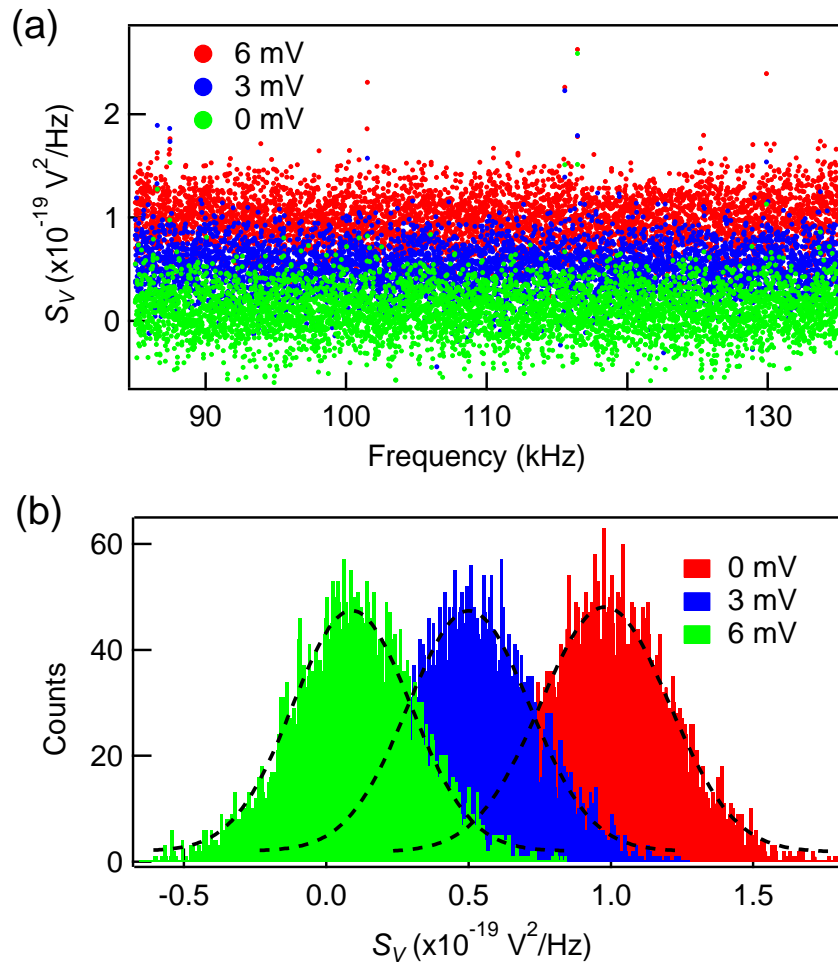
Figure 4.4: (a) Measured voltage noise power spectral density at 0, 2, and 5 mV. (b) Histgram deduced from the voltage noise spectral density in Fig. 4.4(a). The dotted lines are fitted Gaussian function.

Figure 4.5: (a)(b) Differential resistance and current noise power spectral density of MTJs with 1.15 nm thick barrier for the parallel configuration and the antiparallel configuration, respectively. The solid line is the fitting curve and the dashed line represents the curve corresponding to $F = 1$.

Figure 4.6: Dependence of the Fano factor F for the P and AP configurations on the MgO barrier thickness..
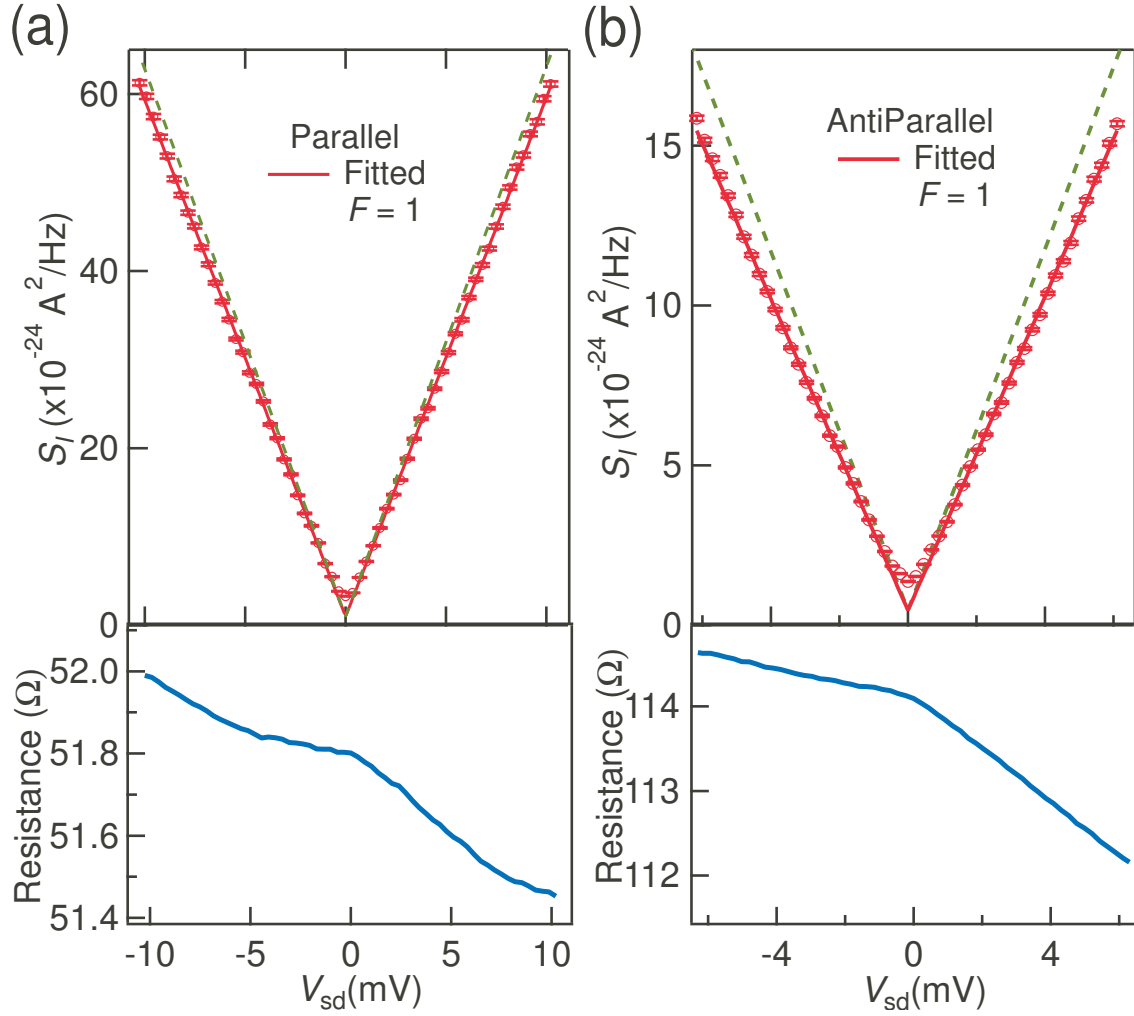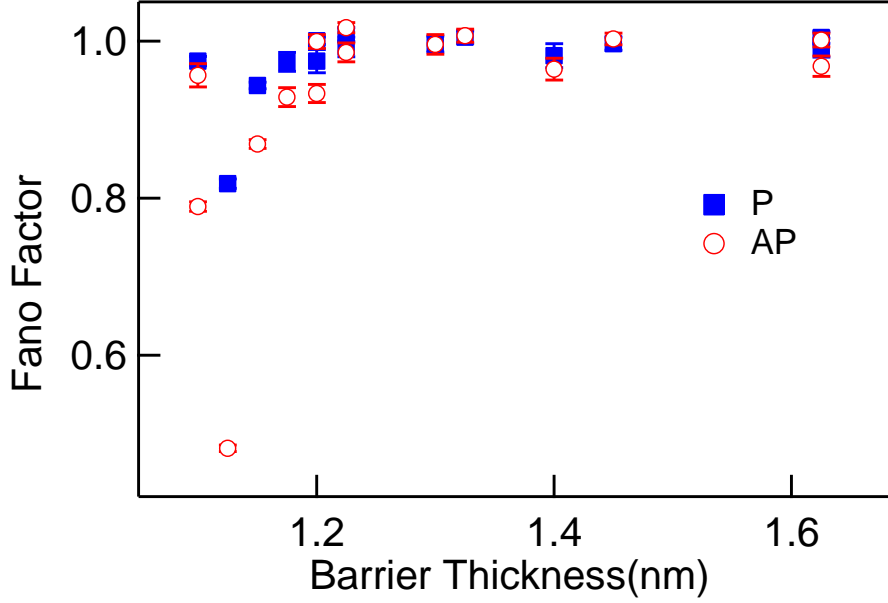
calculations, which cannot be attributed to the coherent tunneling model.

To explain the present result, we assume that the leakage effect due to possible pinholes or defects is responsible for the reduction of F. The fact that the MTJ with 1.125 nm-thick barrier has by far the smallest Fano factor (0.818 ± 0.006 in the P configuration, 0.482 ± 0.004 in the AP configuration) with the lowest RA product ($4.2 \, \Omega \cdot \mu\mathrm{m}^2$) suggests the existence of the leak current and the Fano factor associated with it.

We consider a simple model of the shot noise in the presence of leak current [69]. The effect of the leak current is regarded as a parallel resistance in addition to the intrinsic tunneling resistance as shown in Fig. 4.7. We simply assume that the leak current (parallel resistance) does not depend on the magnetic configurations and that the Fano factor of the leak current is zero as is the case for bulk resistors. That is, the shot noise occurs only due to the current through the tunnel barrier. In this model, the current noise spectrum density and current of MTJs is expressed by the tunnel current (I_t) and the leak current (I_ℓ) as

$$S_I = 2eI_t, \tag{4.1}$$

and

$$I = I_t + I_\ell, \tag{4.2}$$

respectively. The Fano factor is defined as $F = S_I/2eI$ and by substituting S_I and I into F, we can obtain the following by using the intrinsic tunnel conductance $G_{t,\alpha}$ (α is P or
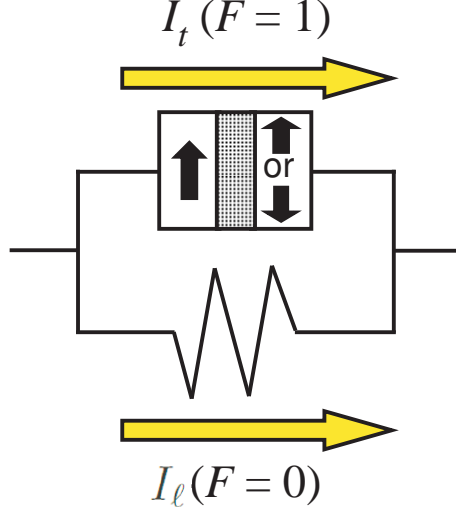
48

Figure 4.7: Schematic picture of the leak current model.

AP),

$$F_\alpha = \frac{G_{t,\alpha}}{G_{t,\alpha} + G_\ell} \tag{4.3}$$

Making use of the above, we deduce the leak conductance (G_ℓ) and the relation of the Fano factor between the P and AP configurations as

$$G_\ell = (1 - F_P)G_P, \tag{4.4}$$

and

$$F_{AP} = 1 - (1 - F_P)\frac{G_P}{G_{AP}}, \tag{4.5}$$

respectively. Here, $G_P = 1/R_P$, and $G_{AP} = 1/R_{AP}$. Now, we can calculate F_{AP} and G_ℓ from the experimental results of F_P, G_P, and G_{AP}.

Figures 4.8(a) and 4.8(b) show the obtained leak conductance G_ℓ and the normalized leak conductance (G_ℓ/G_P) of the measured 15 MTJs. In MTJs with thick barriers, G_ℓ/G_P is negligibly small to be zero within the error bar and leak current does not contribute to the conduction in the MTJs, whereas G_ℓ increases exponentially as barrier thickness decreases. The increase of G_ℓ/G_P as the decrease of the barrier thickness suggests that the leak current makes a significant contribution to the electrical conduction. The result shown in Fig. 4.8(a), namely the quantitative relation between the barrier thickness and the leak current, is the main finding of the present work. Figure 4.9 shows the relation between the calculated Fano factor ($F_{AP,calc}$) and the experimental one ($F_{AP,exp}$). Clearly, $F_{AP,calc}$ quantitatively agrees very well with $F_{AP,exp}$, which supports the validity of this model. Importantly, the leak conductance increases with decreasing t_{MgO}, which agrees well with our empirical knowledge of MTJs.
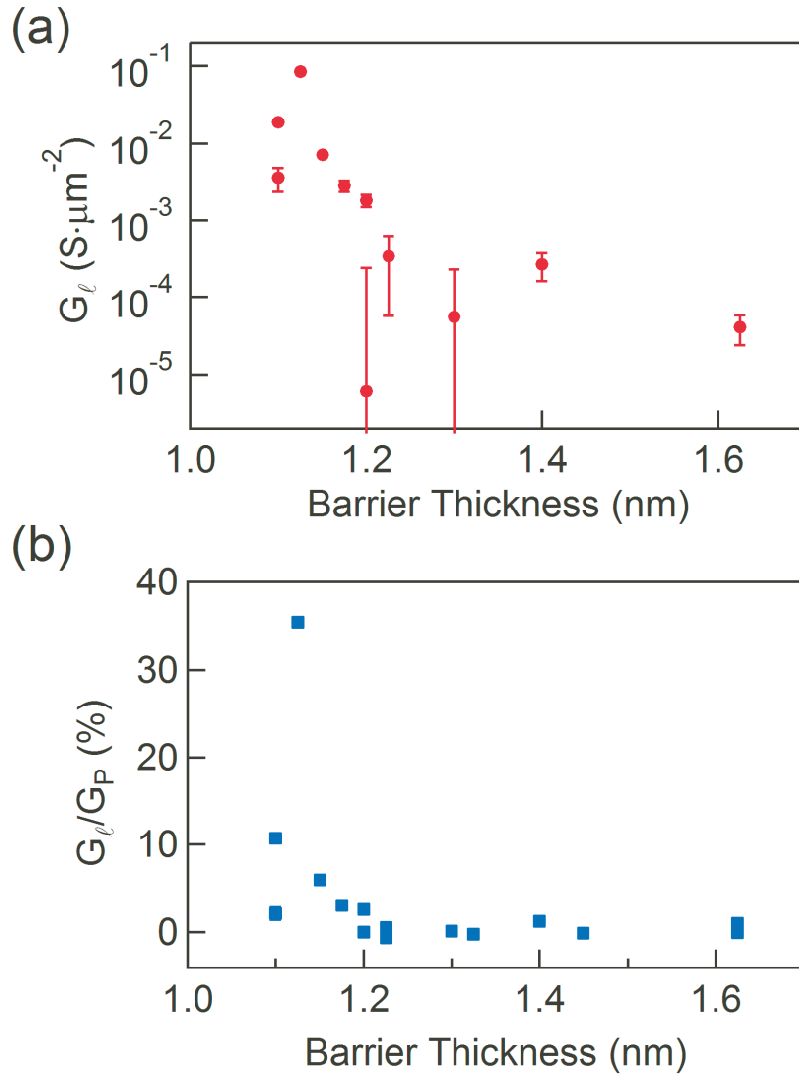
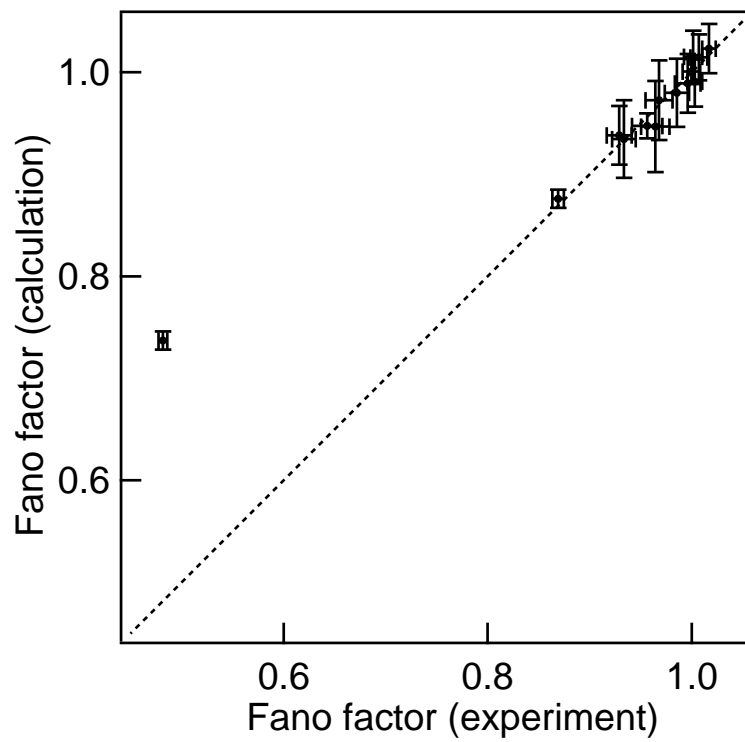Figure 4.8: MgO thickness-dependence of (a) the leak conductance G_ℓ and (b) the normalized leak conductance G_ℓ/G_P.

Figure 4.9: Experimental Fano factor ($F_{\mathrm{AP,exp}}$) versus calculated one ($F_{\mathrm{AP,calc}}$). The dashed line represents $F_{\mathrm{AP,calc}} = F_{\mathrm{AP,exp}}$.
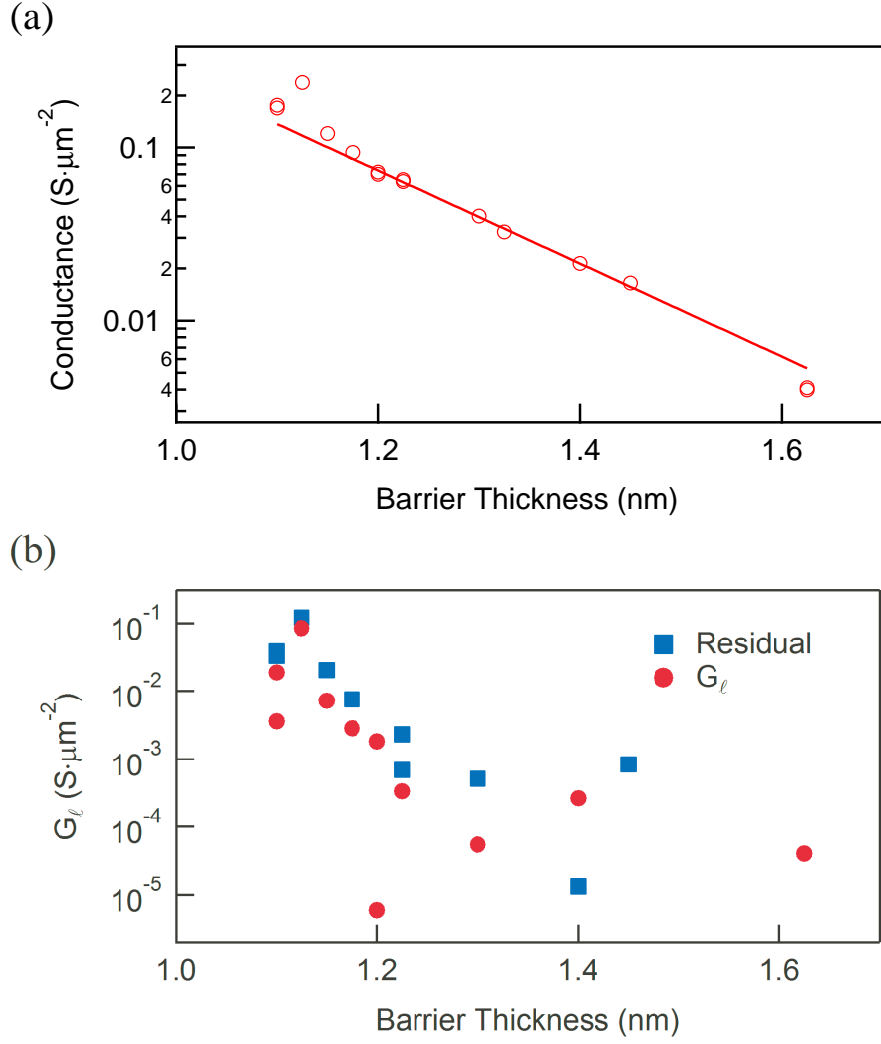
Figure 4.10: (a) Barrier thickness dependence of the conductance per area. Solid line represents the fitted exponential function. (b) The leak conductance derived from the shot noise and the residual of the numerical fitting.

From the dc measurement, we experimentally found that the RA values of the present MTJs slightly deviate from the exponential dependence on the thickness as the barrier thickness decreases below 1.2 nm. The conductance per area (inverse of the RA product) was fitted numerically by exponential function and the residual between the conductance and the fitted line was estimated as shown in Fig. 4.10(a). It should be noted that the numerical fitting is performed by using the conductance of MTJs with $F = 1$. Figure 4.10(b) shows the residual and the leak conductance estimated from the shot noise. These two values show a similar behavior, which constitutes an independent proof of the validity of our model. Importantly, the signal of the leak current is much more prominent in the Fano factor than what is obtained from the RA values.

We note that there are several critical assumptions in the above model. First, the Fano factor of the leak current is set to zero. Second, we take F of the MgO barrier as unity by ignoring the effect of the coherent tunneling. Because of these reasons, the present model may look a simplified one. However, as long as F of the MgO barrier is slightly smaller than 1, the present result is not greatly influenced. It is remarkable that the leak current can be directly estimated by the shot noise measurement to have a clear correlation with the MgO barrier thicknesses. We confirmed that, even if the Fano factor of the leak current component is assumed to be finite rather than zero, the observed tendency remains unchanged. Previously, the coherent tunnel model was discussed by Arakawa *et al.* for the MTJs with a 1.05 nm barrier which have about 200 % MR ratio [24]. The Fano factor was observed to be reproducible from device to device. These results indicate that tunnel barrier is uniform and there is no leak current. The present MTJs do not have comparably large MR ratios and show device-dependent Fano factors. Thus, the MTJs with large MR ratio are necessary to test the coherent tunnel model by the shot noise.

There are other models by which the spin-dependent suppression of the Fano factor with $F_{\mathrm{P}} > F_{\mathrm{AP}}$ could be explained. For example, the spin-dependent tunneling intermediated by the localized impurity state was discussed before [49]. In their model, however, all the electron transports are carried by the sequential tunneling, where the large MR ratio is not expected. The MR ratios of the present MTJs are larger than 100 %, which is not understood by their model.

4.4　Summary

In summary, we measure the shot noise in the MgO-based MTJs. The shot noise with $F_{\mathrm{AP}} < F_{\mathrm{P}}$ is observed in MTJs with thin barrier. From the experimental result that indicates the presence of the leak current, the leak conductance is determined quantitatively by the parallel resistance model. We show that the shot noise measurement is a powerful tool for estimation of the leak current.

t_{MgO} (nm)	JA (nm^2)	RA ($\Omega \cdot \mu\mathrm{m}^2$)	MR ratio (%)	F_{P}	F_{AP}
1.1	200×800	5.7	97.2 (1.6 K)		0.790 ± 0.006
1.1	200×800	5.9	105.3 (4 K)	0.974 ± 0.006	0.956 ± 0.015
1.125	200×800	4.2	44.7 (1.6 K)	0.818 ± 0.006	0.482 ± 0.005
1.15	200×800	8.3	120.2 (1.6 K)	0.944 ± 0.005	0.869 ± 0.006
1.175	200×800	10.7	134.7 (4 K)	0.974 ± 0.013	0.929 ± 0.013
1.2	200×800	14.3	154.4 (4 K)	0.974 ± 0.015	0.933 ± 0.012
1.2	200×800	13.9	170.1 (1.6 K)	1.000 ± 0.005	1.000 ± 0.009
1.225	200×800	15.7	171.8 (4 K)	0.993 ± 0.013	0.986 ± 0.012
1.225	200×800	15.3	176.5 (1.6 K)	1.008 ± 0.009	1.017 ± 0.007
1.3	200×800	24.9	189.7 (4 K)	0.996 ± 0.010	0.996 ± 0.013
1.325	200×800	30.5	190.2 (1.6 K)	1.005 ± 0.008	1.007 ± 0.009
1.4	200×800	46.7	190.6 (4 K)	0.982 ± 0.016	0.964 ± 0.014
1.45	200×800	60.6	201.6 (1.6 K)	0.997 ± 0.009	1.003 ± 0.008
1.625	500×2000	244.4	221.2 (4 K)	0.992 ± 0.013	0.968 ± 0.014
1.625	500×2000	251.8	240.2 (1.6 K)	1.005 ± 0.008	1.001 ± 0.009

Table 4.1: Characteristics and Fano factor of the MgO-based MTJs studied in this work.

Chapter 5

Ballistic detector for magnetic vortex core

5.1 Background

In Chapter 1, the macroscopic quantum tunneling (MQT) was introduced. The MQT is a phenomenon that the macroscopic object transmits a potential barrier by the quantum tunnel process. The MQT in the ferromagnets was reported [31–34], and attracts an interest from a point of view on whether the macroscopic spin system, namely the ferromagnet, can tunnel or not. In this work, we focus on the magnetic vortex core [72]. In order to test the MQT in the magnetic vortex core, we require the detector for the magnetic vortex core. In this Chapter, we explore the potential of a microcavity fabricated in two dimensional electron gas as the ballistic detector of the vortex core by the method of billiard simulation [73].

5.1.1 Magnetic vortex

The magnetic structure of ferromagnet is determined to minimize the free energy, which is the sum of magnetostatic energy, magnetic anisotropy energy, and exchange energy. Generally, the ferromagnet is demagnetized by taking multi-magnetic-domain structure with different directions of magnetization to lower the magnetostatic energy [74]. There is a transition region between two magnetic domains called domain wall, where electron spins rotate gradually across a finite distance. However, when the ferromagnet becomes submicroscale, the instability of forming the domain wall becomes larger. Consequently, the submicroscale ferromagnet often exists only as a single domain.

In the submicroscale ferromagnet, the magnetic structure depends on the shape and size. The ferromagnetic dot forms the magnetic vortex structure, where spin directions change gradually in-plane [72]. Figure 5.1(a) shows the structure of magnetic vortex. This

structure originates from the competition between magnetostatic energy and exchange energy. At the center of the disk, the direction of spins becomes out-of-plane to prevent exchange energy from increasing rapidly due to smaller angle between adjacent spins. The direction of out-of-plane spins is called polarity of the vortex core. The size of vortex core is about 10 nm. As is clear from Fig. 5.1(a), in addition to polarity the disk has another degree of freedom, namely, the chirality, which is the rotating direction of the magnetic vortex. However, in this Chapter, we only focus on the polarity of the magnetic core.

At zero magnetic field, the magnetic vortexes with up polarity and down polarity have the same energy. There exists a potential barrier between the two states as shown in Fig. 5.1(b). When a out-of-plane magnetic field is applied to the magnetic vortex, the magnetic vortex with a polarity parallel to the magnetic field is more stable than that with the other polarity. At a certain magnetic field, the magnetic vortex core is reversed by exceeding the potential barrier.

As described above, the spin tunneling is not unusual at low temperature and have been discussed [75]. The magnetic vortex core is one of the candidates for the MQT. The vortex core behaves collaboratively because of the strong exchange interaction and is nanoscopic size (10 nm). The quantum depinning of the magnetic vortex core is reported [76]. Therefore, the vortex core might show the quantum tunneling between the up and down polarities.

Usually, the polarity of the vortex core is measured by the magnetic force microscopy (MFM) [72]. However, the MFM is invasive and may change the polarity of the core. The MFM also takes a long time to detect the polarity of the vortex core. A another good magnetic sensor, superconducting quantum interference device (SQUID) is weak to the magnetic field. In this thesis, we focus on the microcavity fabricated in the 2DEG.

5.1.2 Two dimensional electron gas [7]

Two dimensional electron gas (2DEG) is a research target with good controllability, where many studies about quantum Hall effect [77–79], quantum dot [80,81] and so on are carried out. The ballistic detector in this is also fabricated in the 2DEG. Here, the typical 2DEG, GaAs/AlGaAs heterojunction, is explained.

2DEG is formed at the interface between two semiconductor materials with different band gap (,however, other properties such as lattice constant are similar, which in needed for manufacturing heterostructure). Figure 5.2(a) shows the band diagram of the non-doped GaAs/n-type AlGaAs heterojunction. The Fermi energy E_{F} in the n-type AlGaAs is higher than that in the non-doped GaAs. Consequently, electrons transfer from AlGaAs to GaAs leaving behind positively charged donors. This polarization prevents the charge transfer. At equilibrium, the Fermi energies in AlGaAs and GaAs are the same as shown in Fig. 5.2(b). The electrons spilled over from the n-type AlGaAs are restrained in the
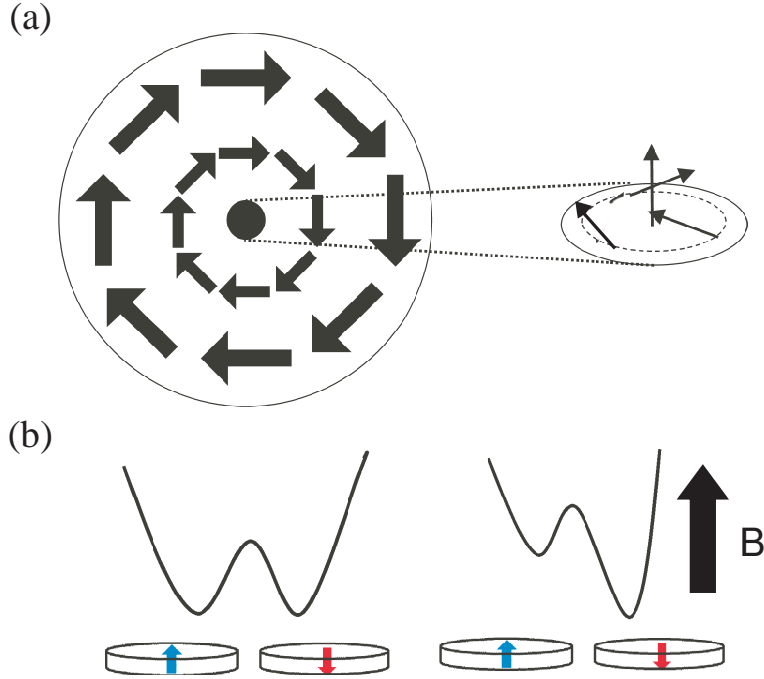
Figure 5.1: (a) Magnetic structure of magnetic vortex. (b) Schematic image of the potential barrier between the magnetic vortexes with up and down polarity.

GaAs near the interface between AlGaAs and GaAs and form 2DEG. 2DEG in GaAs is separated spatially from donors in AlGaAs, which suppresses the scattering due to the impurities and defects. In the 2DEG, the mean free path reaches a few μm and the electron transport becomes ballistic.

5.1.3 Ballistic detector

In 2DEG, various structures such as quantum dot and quantum point contact are formed by the split gate method. Microcavity is a typical example, where electrons are confined in a microscale dot as shown in the inset of Fig. 5.3(a) [82]. It is mainly used as an optical device [83], however, it also shows interesting electrical transport. At very low temperature, weak localization and universal conductance fluctuation give sharp features in the magnetoresistance as shown in Fig. 5.3(a) [82,84]. In this system, the conductance is well described by billiard model simulation explained below [85].

In this Chapter, the microcavity is used for the ballistic detector. Figure 5.3(b) shows the schematic image of the ballistic detector. The magnetic vortex is fabricated just above the microcavity in 2DEG. Electrons transporting in the microcavity are expected to be affected by the stray field from the magnetic vortex core; The electrons go backward and forward many times in the microcavity and the effect of stray field would become larger. It may enable us to detect the change in the conductance due to the stray field.
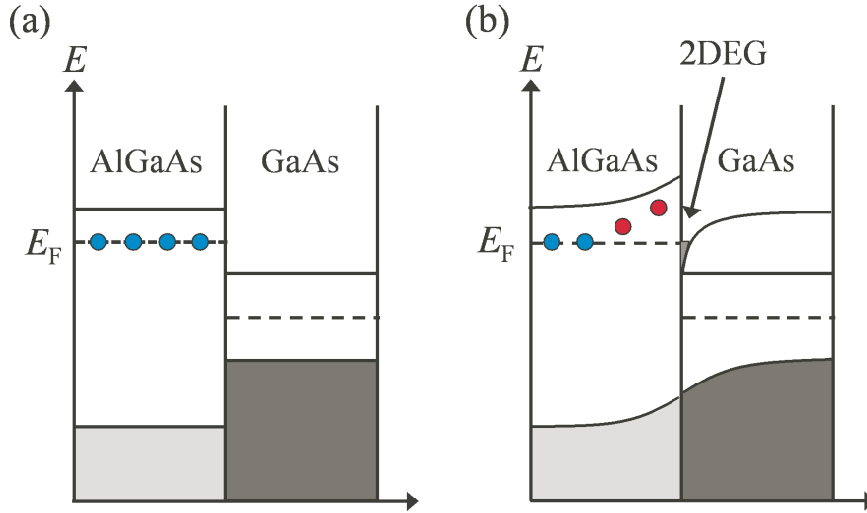
Figure 5.2: Band diagram of the non-doped GaAs/n-type AlGaAs heterojunction (a) before and (b) after charge transfer has taken place.

If the conductance changes depending on the polarity of the magnetic vortex core, we can detect the polarity over wide range of temperature and external magnetic field. In order to determine the value of magnetic field at which vortex core reverses, the magnetic field dependence of the resistance should be measured. If the resistance has a hysteresis depending on the polarity of the magnetic vortex core, we can determine the value of magnetic field for core reversal from the hysteresis loop.

5.2 Billiard simulation

5.2.1 Billiard model [86]

In order to explore the potential of the ballistic detector, we performed the classical billiard simulation which is useful for investigation of the transport in the microcavity. In this model, the electrons are treated as the mass points and are elastically scattered many times by the wall of the microcavity (billiard table) like billiard balls. Here, quantum effects such as interferences are ignored. Due to it, the classical billiard model is invalid at the very low temperature. However, the sensitivity of ballistic detector might increase when the quantum effects arises. If the classical ballistic detector can detect the reversal of magnetic vortex core, it is useful over the higher range of temperature where quantum effect is not significant..
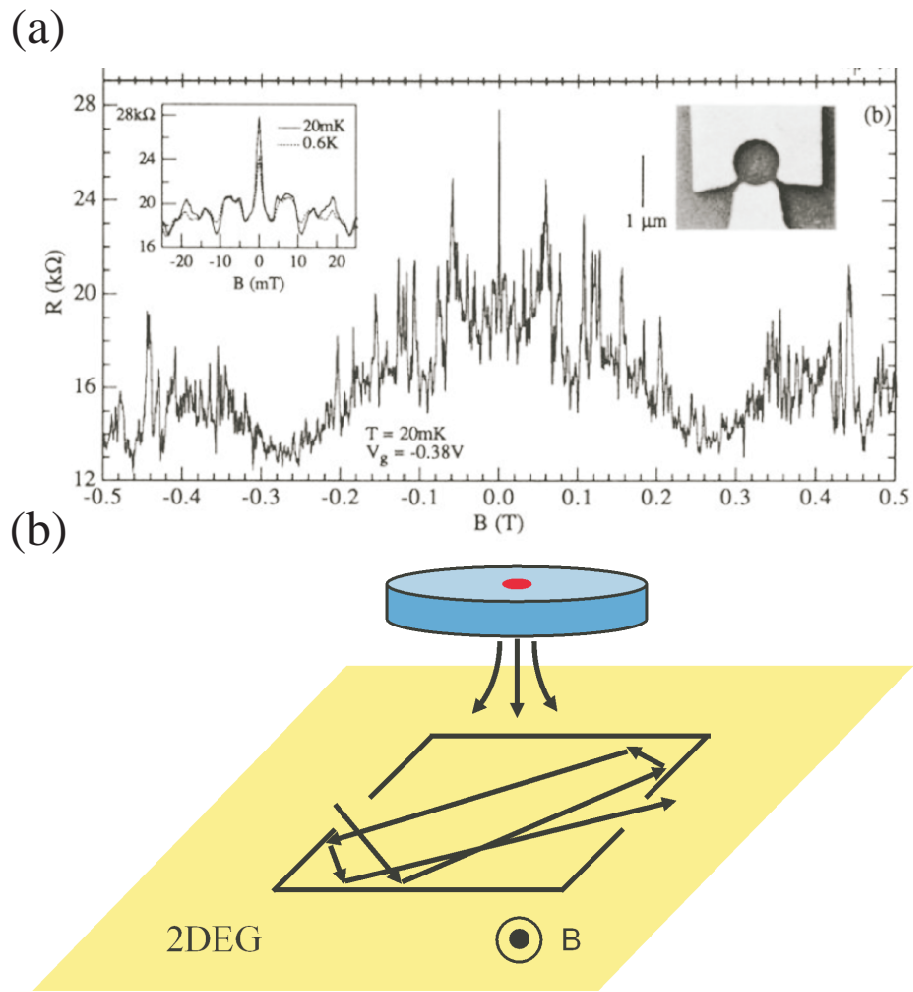
(a)

(b)

Figure 5.3: (a)Magnetoresistance of the microcavity [82]. (b) Schematic picture of the ballistic detector, which we treat in this Chapter.

5.2.2 Calculation method

We calculated the transmission probability T for the both polarity and the change in T defined as $\Delta T = (T_\uparrow - T_\downarrow)/T_\uparrow$ in the range of external magnetic field from 0.05 T to 0.4 T by using following condition and method. Here, $T_\uparrow$ and $T_\downarrow$ are the transmission probabilities for up and down polarity, respectively.

Calculation condition

The shape of the microcavity is set as a square of $1 \times 1 \ \mu m^2$ with 50 nm entrance and exit at the center of left and right edge, respectively, as shown Fig 5.5. We injected 10^6 electrons with various positions and angles of the incidence (1000 position: -25 nm $< x < 25$ nm, 1000 angle: $-90° < \theta < 90°$). The velocity of electron is $3.0 \times 10^5 m/s$ which is a Fermi velocity in a typical 2DEG.. The distance between 2DEG and the surface of magnetic vortex is 60 nm. The stray field from magnetic vortex is calculated by Yoshinobu Nakatani and Keisuke Yamada in University of Electro-Communications. This magnetic field is calculated by summing the stray field from the magnetic vortex which is divided into cells. Here, the thickness of the magnetic disk is 50 nm. Figures 5.4(a) and 5.4(b) show the stray field from the magnetic vortex and the line profile at $y = 0$. The stray field at just above magnetic vortex core is about 5 mT and spreads about 100 nm. We approximate the stray field by a step function as shown in Fig. 5.4(b) in order to simplify the calculation.
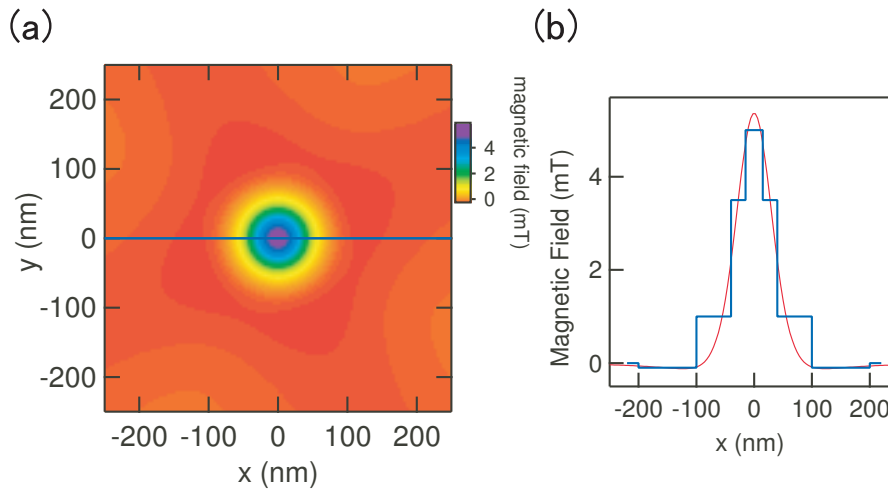
(a)   (b)

Figure 5.4: (a)Magnetic field distribution from magnetic vortex core at the plane 60 nm away from the surface of magnetic vortex (b) Red line is the lineprofile of Fig. 5.4(a) at $y = 0$. The blue line is the approximate step function.

Calculation method

We calculated whether electrons transmit or are reflected by the following method.

1. We calculated the cyclotron motion from the initial conditions, position and angle of incidence, velocity and external magnetic field.

2. We calculated a collision point between electron and ballistic detector and also calculated the cyclotron motion after the elastic collision.

3. When the electron enters the region of stray field (red circle), the cyclotron radius changes depending on the stray field from magnetic vortex core.

4. When the electron touches the entrance or exit of the ballistic detector, we count it as transmission or reflection respectively.
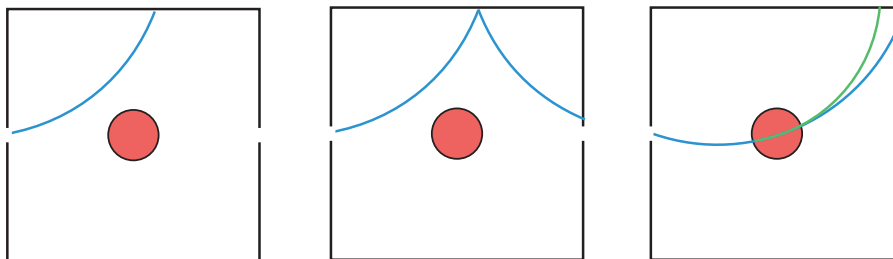
Figure 5.5: Schematic illustration of the calculation method.

5.3   Result and discussion

5.3.1   Transmission probability

First, we assumed that the stray field is a circular region of 10 mT with 100 nm-radius and calculated the trajectories of electrons for both polarity in the external magnetic field as large as 0.2 T as shown in Fig. 5.6. At first, electrons for both polarity moves in a same trajectory. However, once electrons passed the stray field region, these trajectories slightly change. After electrons are reflected in the microcavity many times and pass stray field region sometimes, these trajectories become completely different. Finally, the electron for up polarity transmitted, while the electron for down polarity was reflected. It was found that the electrons transporting the microcavity are affected by stray field from magnetic vortex.

Figures 5.7(a) and 5.7(b) show the magnetic field dependence of transmission probability for both polarities and ΔT. Transmission probability oscillates as a function of the external magnetic field. ΔT is typically 3 % and at most 5 %, which would be experimentally detectable value. We also calculated the stray field dependence of T and ΔT in
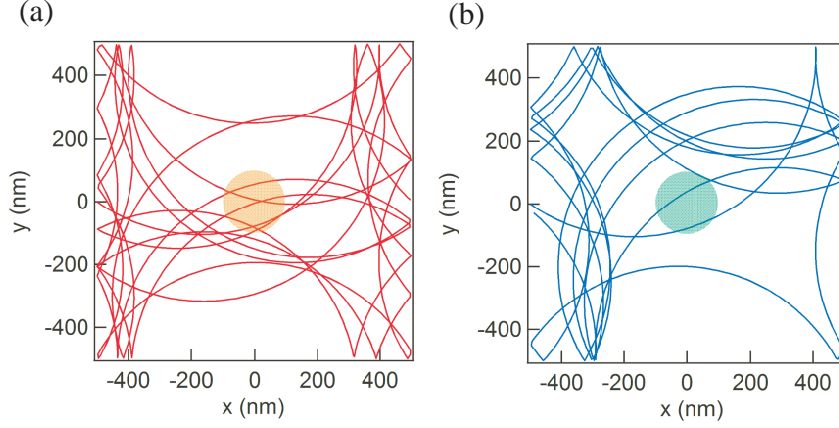
61

Figure 5.6: Trajectories of electrons for (a) up polarity and (b) down polarity.

the external magnetic field of 0.45 T as shown in Figs. 5.8(a) and 5.8(b). The stray field is assumed to be a circle with a radius as large as 100 nm. Although $T_\uparrow$ decreases with increasing stray magnetic field, $T_\downarrow$ increases monotonically. Consequently, ΔT increases up to 6 % and ΔT at different external magnetic field also tends to increase with increasing stray magnetic field. These results indicate that the ballistic detector works as a detector of the polarity of magnetic vortex core in principle.

Figures 5.9(a) and 5.9(b) show the magnetic field dependence of transmission probability for the both polarities and ΔT, where calculated stray field (1 mT - 5 mT) was used for the billiard simulation. T oscillates as a function of magnetic field as well as the case of assumed stray field. T slightly depends on the polarity and ΔT is typically 0.3 %. The maximum value of ΔT is 3 % at 0.2 T. These values are much smaller than ΔT for assumed stray field. In order to detect the polarity, we must measure the conductance precisely.

5.4   Summary

We focus on the microcavity fabricated in 2DEG and investigate the potential of the microcavity as the detector for the magnetic vortex core. We calculated the transmission probability T of the microcavity by the method of the classical billiard simulation. T depends on the polarity of the vortex core and ΔT tends to increase with increasing stray field of vortex core, which indicates that the microcavity can detect the polarity of the magnetic vortex core in principle. For the calculated stray field, ΔT is typically 0.3 % and is 3 % at most. We might be able to detect the polarity through the precise measurement, which leads to the experimental test of the MQT in the magnetic vortex core.

Figure 5.7: Magnetic field dependence of (a) the transmission probability of the micro-cavity for up and down polarity and (b) ΔT for the stray field of 10 mT.
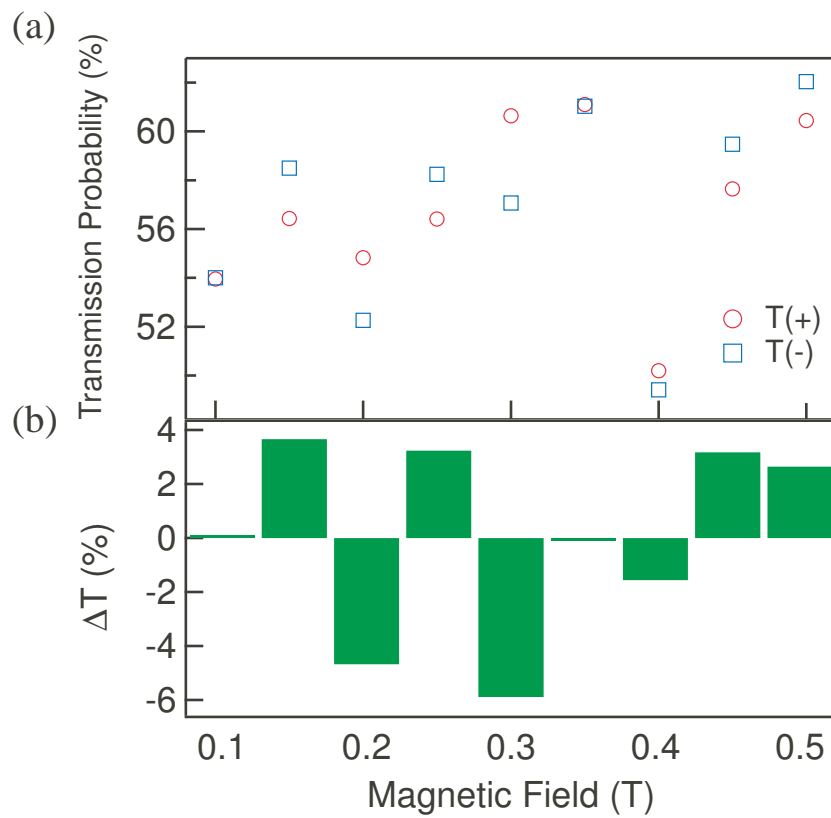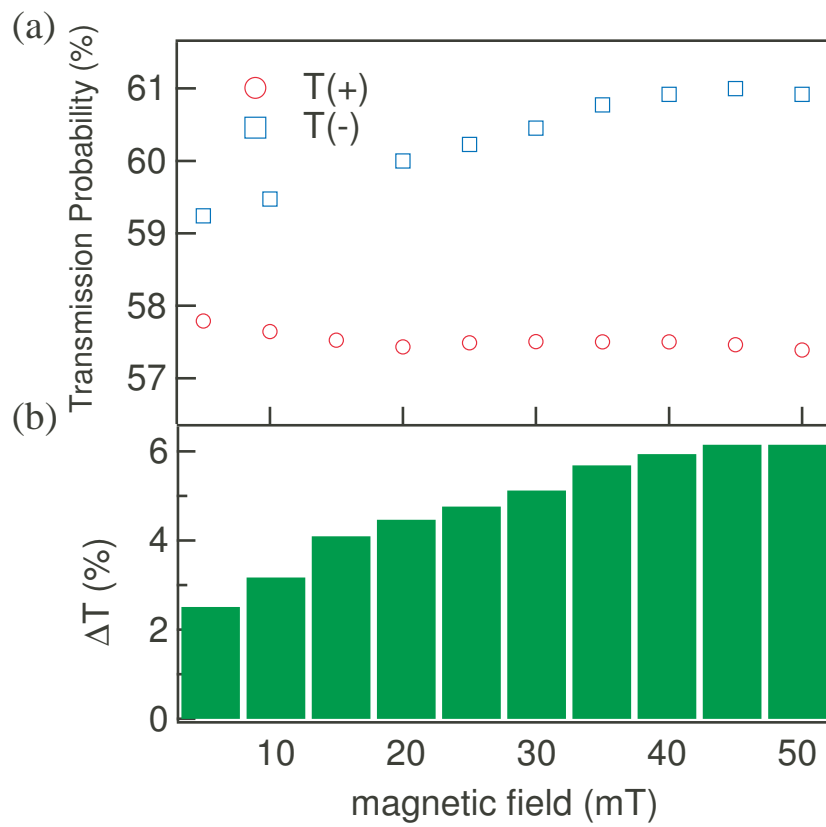
Figure 5.8: Stray field dependence of (a) the transmission probability of the microcavity for up and down polarity and (b) ΔT.
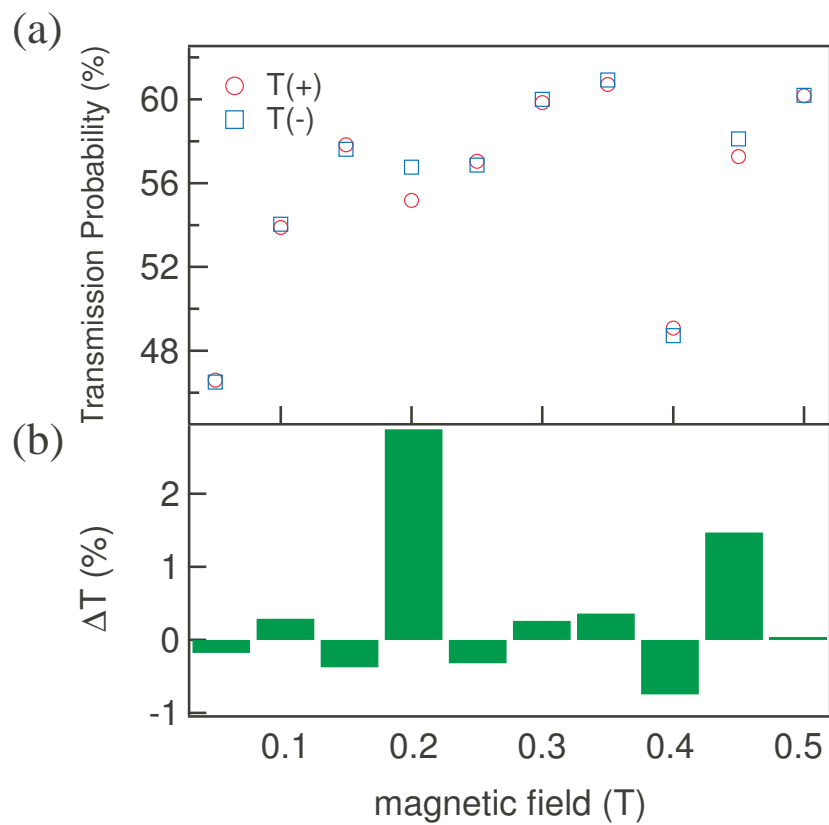
Figure 5.9: Magnetic field dependence of (a) transmission probability of the ballistic detector for up and down polarity and (b) ΔT in the case of calculated stray field.

Chapter 6

Summary

Here, we summarize the results of this Thesis where, we investigated the tunnel phenomena in submicroscale ferromagnetic systems.

Coherent tunneling in spinel-based MTJs

We measured the shot noise in nine spinel-based MTJs with the thin and thick barriers and different junction areas and evaluated the Fano factor F. When the barrier is thick, the Poissonian shot noise is observed for both of P and AP configuration. On the other hand, in the MTJs with a thin barrier, the shot noise is suppressed for the P configuration (typically $F = 0.98$) although the Fano factor for the AP configuration equals to unity. In the present MTJs, the Fano factor does not depend on the junction area, which means that these observations are intrinsic in the present MTJs. The present results are qualitatively agree with the results in the MgO-based MTJs [24, 53]. It supports that the coherent tunneling model is valid in the spinel-based MTJs as well as MgO-based MTJs. We also measured the $1/f$ noise. The Hooge parameters α are typically $1 - 5 \times 10^{-12}$ (μm^2) for the P configuration and $2 - 9 \times 10^{-11}$ (μm^2) for the AP configuration, which is consistent with the previous results. For all the MTJs, α is larger in the AP configuration than that in the P configuration, as is usually the case in MTJs [45, 48, 54–63]. It indicates that one of the origins of the $1/f$ noise in the spinel-based MTJs is the thermal fluctuation of the magnetization.

Microscopic tunnel processes in MgO-based MTJs

We measured the shot noise in 15 MgO-based MTJs with various barrier thickness t_{MgO}. When the barrier is thick ($t_{MgO} > 1.2$ nm), the Fano factor is very close to 1 for both configurations. In contrast, in the MTJs with a thin barrier ($t_{MgO} < 1.2$ nm), F decreases with decreasing t_{MgO}. Furthermore, F for the AP configuration is smaller than that for the P configuration. We explain this result by the simple parallel resistance model in the presence of the leak current. The leak current was estimated from the shot noise and is

enhanced exponentially with decreasing t_{MgO}. The calculated Fano factor from the model is in good agreement with the experimental Fano facor, which means that this model well describes the present situation. This work shows that the shot noise is a powerful tool for the quantitative estimation of the leak current.

Ballistic detector for magnetic vortex core

We focus on the microcavity as the detector for the magnetic vortex core. We confirmed that the trajectory of the electron transporting in the microcavity is affected by the stray field from the magnetic vortex. We calculated the transmission probability T of the microcavity by the method of the classical billiard simulation. T depends on the polarity of the vortex core, which indicates that the microcavity can detect the polarity of the magnetic vortex core in principle. For the calculated stray field, ΔT is typically 0.3 % and is 3 % at most. We could detect the polarity through the precise conductance measurement.

In this thesis, we clarify the tunnel process by the various methods, establish and propose the methods for investigation the tunnel processes through the three studies.

Future perspective

The shot noise measurement is the useful tool for addressing the conduction process in tunnel junctions and expected to be applied in various tunnel junctions. It is also worth trying to detect the polarity of the magnetic vortex core by the ballistic detector experimentally, which leads to the experimental test of the MQT in a single magnetic vortex core.

謝辞

本研究を進めるにあたり、多くの方々にお世話になりました。

小林研介教授には、長い間研究ことから進路まで様々なご指導をしていただきました。また、小林先生の前向きな姿勢にはいつも助けられるとともに見習いたいと考えています。本当に感謝しております。

京都大学の小野輝男教授には、小野研を卒業してからもいつも気にかけていただきました。小野先生には優しく、時に厳しく研究者としてあるべき姿を教えていただきました。

新見康洋准教授には研究へのスタンスなど研究者として目指すべき姿を見せていただきました。

荒川智紀助教には実験技術や解析について一から教えていただきました。私が研究で悩んだ時には的確な助言をしていただきたことを深く感謝しております。

田辺賢士特任助教（現名古屋大学）には隣で研究に没頭する姿に刺激を頂いていました。

故那須三郎大阪大学名誉教授にはいつも楽しい話を聞かせていただきました。ご冥福をお祈りいたします。

共同研究者である三谷誠司博士、介川裕章博士、葛西伸哉博士には大変質の良い試料を提供していただき、本当に感謝しております。おかげ様で、良い実験を行うことができました。

湯浅新治博士、福島章雄博士、野崎隆行博士には大変質の良い試料を提供していただきました。また試料の微細加工にもご協力して下さいました。本当に感謝しております。

秘書の由良利子さん、佐々木潤子には事務の仕事でお世話になりました。由良さんには大阪大学に来たばかりで不慣れな私を助けて下さいました。

小野研究室でお世話になった千葉大地准教授、Kab-jin Kim 助教、森山貴広助教、卒業生、学生の皆様には大変お世話になりました。先輩である知田健作博士、松尾貞茂博士、西原禎孝博士とは研究を進める上で様々な助言をいただき、また研究以外にも様々な話をしていただき楽しい研究室生活を送ることができました。また同期である河口真志君と吉村瑶子さんとは、学会で会うたびに様々な話をし、刺激となりました。

小林研究室のポスドクの吉井涼輔博士、学生の皆様には実験にご協力いただきました。吉井さんには楽しい話を聞かせていただき、また囲碁を教えていただきました。特に、秦徳郎君、前田正博君、竹下俊平君、室達也君、横井雅彦君、河村智也君とは実験について色々と手伝っていただきました。皆様と一緒に実験できたことに嬉しく思います。皆様の

おかげで大阪大学でも楽しく過ごすことができました。感謝しております。

　パリ南大学の Meydi Ferrier 博士には物理を深く追求する姿を見せていただきました。フランスから持ってきてくださったフォアグラは本当に美味しかったです。

　最後になりますが、大学院生活を支えて下さった家族に心より感謝いたします。

Reference

[1] 栗原 進編, シリーズ物性物理の新展開「トンネル効果」 丸善 (1994).

[2] L. Esaki, New Phenomenon in Narrow Germanium *p-n* Junctions. *Phys. Rev.* **109**, 603 (1958).

[3] B. D. Josephson, Possible new effects in superconductive tunnelling.*Phys. Lett.* **1**, 251 (1962).

[4] I. Giaever, Electron Tunneling Between Two Superconductors. *Phys. Rev. Lett.* **5**, 464 (1960).

[5] A. J. Leggett, Testing the limits of quantum mechanics: motivation, state of play, prospects. *J. Phys.: Condens. Matter.* **14**, R415 (2002).

[6] S. Yuasa, Giant Tunneling Magnetoresistance in MgO-Based Magnetic Tunnel Junctions. *J. Phys. Soc. Jpn.* **77**, 031001 (2008).

[7] S. Datta, Electronic Tranport in Mesoscopic Systems. Cambridge Univ. Press (1997).

[8] M. Julliere, Tunneling between ferromagnetic films. *Phys. Lett.* **54A**, 225 (1975).

[9] W. H. Butler, X.-G. Zhang, T. C. Schulthess, and J. M. MacLaren, Spin-dependent tunneling conductance of Fe/MgO/Fe sandwiches. *Phys. Rev. B* **63**, 054416 (2001).

[10] J. Mathon and A. Umerski, Theory of tunneling magnetoresistance of an epitaxial Fe/MgO/Fe(001) junction. *Phys. Rev.* B, **63**, 220403(R) (2001).

[11] M. N. Baibich, J. M. Broto, A. Fert, F. Nguyen Van Dau, F. Petroff, P. Eitenne, G. Creuzet, A. Friederich, and J. Chazelas, Giant magnetoresistance of (001)Fe/(001)Cr magnetic superlattices. *Phys. Rev. Lett.* **61**, 2472 (1988).

[12] G. Binasch, P. Griinberg, F. Saurenbach, and W. Zinn, Enhanced magnetoresistance in layered magnetic structures with antiferromagnetic interlayer exchange. *Phys. Rev. B* **39**, 4828 (1989).

[13] T. Miyazaki and N. Tezuka, Giant magnetic tunneling effect in Fe/Al2O3/Fe junction. *J. Magn. Magn. Mater.* **139**, L231 (1995).

[14] J. S. Moodera, Lisa R. Kinder, Terrilyn M. Wong, and R. Meservey, Large magnetoresistance at room temperature in ferromagnetic thin film tunnel junctions. *Phys. Rev. Lett.* **74**, 3273 (1995).

[15] S. Yuasa, T. Nagahama, A. Fukushima, Y. Suzuki and K. Ando, Giant room-temperature magnetoresistance in single-crystal Fe/MgO/Fe magnetic tunnel junctions/ *Nat. Mater.* **3**, 868 (2004).

[16] S. S. P. Parkin, C. Kaiser, A. Panchula, P. M. Rice, B. Hughes, M. Samant, and S.-H. Yang, Giant tunnelling magnetoresistance at room temperature with MgO (100) tunnel barriers. *Nat. Mater.* **3**, 862 (2004).

[17] Shinji Yuasa, Akio Fukushima, Hitoshi Kubota, Yoshishige Suzuki, and Koji Ando, Giant tunneling magnetoresistance up to 410 % at room temperature in fully epitaxial CoMgOCo magnetic tunnel junctions with bcc Co(001) electrodes. *Appl. Phys. Lett.* **89**, 042505 (2006).

[18] Y. Taniguchi , Y. Miura , K. Abe, and M. Shirai , Theoretical Studies on Spin-Dependent Conductance in FePt/MgO/FePt(001) Magnetic Tunnel Junctions. *IEEE Trans. Magn.*, **44** 2585 (2008).

[19] Y. Miura, H. Uchida, Y. Oba, K. Nagao, and M. Shirai, Coherent tunnelling conductance in magnetic tunnel junctions of half-metallic full Heusler alloys with MgO barriers. *J. Phys.: Condens. Matter.* **19**, 365228 (2007).

[20] H. Sukegawa, H. Xiu, T. Ohkubo, T. Furubayashi, T. Niizeki, W. Wang, S. Kasai, S. Mitani, K. Inomata, and K. Hono, Tunnel magnetoresistance with improved bias voltage dependence in lattice-matched Fe/spinel $MgAl_2O_4$/Fe(001) junctions. *Appl. Phys. Lett.* **96**, 212505 (2010).

[21] H. Sukegawa, Y. Miura, S. Muramoto, S. Mitani, T. Niizeki, T. Ohkubo, K. Abe, M. Shirai, K. Inomata, and K. Hono, Enhanced tunnel magnetoresistance in a spinel oxide barrier with cation-site disorder. *Phys. Rev. B* **86**, 184401 (2012).

[22] R. Meservey and P. M. Tedrow, Spin-polarized electron tunneling. *Phys. Rep.* **238**, 173 (1994).

[23] R. Matsumoto, A. Fukushima, T. Nagahama, Y. Suzuki, K. Ando, and S. Yuasa, Oscillation of giant tunneling magnetoresistance with respect to tunneling barrier thickness in fully epitaxial Fe/MgO/Fe magnetic tunnel junctions. *Appl. Phys. Lett.* **90**, 252506 (2007).

[24] T. Arakawa, K. Sekiguchi, S. Nakamura, K. Chida, Y. Nishihara, D. Chiba, K. Kobayashi, A. Fukushima, S. Yuasa, and T. Ono, Sub-Poissonian shot noise in CoFeB/MgO/CoFeB-based magnetic tunneling junctions. *Appl. Phys. Lett.* **98**, 202103 (2011).

[25] E. M. Chudnovsky and J. Tejada, Macroscopic Quantum Tunneling of the Magnetic Moment. Cambridge Univ. Press (2005).

[26] 多々良 源，　巨視的量子トンネル現象 (41 回物性若手夏の学校講義ノート) (1996).

[27] Richard F. Voss and Richard A. Webb, Macroscopic quantum tunneling in 1-μm Nb Josephson junctions. *Phys. Rev. Lett.* **47**, 265 (1981).

[28] J. M. Martinis, M. H. Devoret and J. Clarke,Energy-Level Quantization in the Zero-Voltage State of a Current-Biased Josephson Junction. *Phys. Rev. Lett.* **55**, 1543 (1985).

[29] R. Rouse, Siyuan Han, and J.E. Lukens, Observation of Resonant Tunneling between Macroscopically Distinct Quantum Levels. *Phys. Rev. Lett.* **75**, 1614 (1995).

[30] I. Chiorescu, Y. Nakamura, C. J. P. M. Harmans and J. E. Mooij, Coherent Quantum Dynamics of a Superconducting Flux Qubit. *Science* **299**, 1869 (2003).

[31] J. Brooke, T. F. Rosenbaum and G. Aeppli, Tunable quantum tunnelling of magnetic domainwalls. *Nature* **413**, 610 (2001).

[32] G. Tatara and H. Fukuyama, Macroscopic Quantum Tunneling of a Domain Wall in a Ferromagnetic Metal. *Phys. Rev. Lett.* **72**, 772 (1994).

[33] W. Wernsdorfer, B. Doudin, D. Mailly, K. Hasselbach, A. Benoit, J. Meier, J. -Ph. Ansermet, and B. Barbara, Nucleation of Magnetization Reversal in Individual Nanosized Nickel Wires. *Phys. Rev. Lett.* **77**, 1873 (1996).

[34] Jonathan R. Fried42man, M. P. Sarachik, J. Tejada, and R. Ziolo, Macroscopic Measurement of Resonant Magnetization Tunneling in High-Spin Molecules. *Phys. Rev. Lett.* **76**, 3830 (1996).

[35] A. O. Caldeira and A. J. Leggett, Influence of Dissipation on Quantum Tunneling in Macroscopic Systems. *Phys. Rev. Lett.* **46**, 211 (1981).

[36] Y. M. Blanter and M. B. Büttiker, Shot noise in mesoscopic conductors. *Phys. Rep.* **336**, 1 (2000).

[37] J. B. Johnson, Thermal Agitation of Electricity in Conductors. *Phys. Lett.* **32**, 97 (1928).

[38] H. Nyquist, Thermal agitation of electric charge in conductors. *Phys. Rev.* **32**, 110 (1928).

[39] L. Spietz, K. W. Lehnert, I. Siddiqi, R. J. Schoelkopf, Primary Electronic Thermometry Using the Shot Noise of a Tunnel Junction. *Science* **300**, 1929 (2003).

[40] F. N. Hooge, T. G. M. Kleinpenning and L. K. J. Vandamme, Experimental studies on $1/f$ noise. textitRep. Ping. Phys. **44**, 479 (1981).

[41] X. Jehl, M. Sanquer, R. Calemczuk and D. Mailly, Detection of doubled shot noise in short normal-metal/ superconductor junctions. *Nature* **405**, 50 (2000).

[42] R. de-Picciotto, M. Reznikov, M. Heiblum, V. Umansky, G. Bunin and D. Mahalu, Direct observation of a fractional charge. *Nature.* **389**, 162 (1997).

[43] L. Saminadayar and D. C. Glattli, Observation of the $e/3$ Fractionally Charged Laughlin Quasiparticle. *Phys. Rev. Lett.* **79**, 2526 (1997).

[44] A. Kumar, L. Saminadayar, D. C. Glattli, Y. Jin and B. Etienne, Experimental Test of the Quantum Shot Noise Reduction Theory. *Phys. Rev. Lett.* **76**, 2778 (1996).

[45] T. Arakawa, T. Tanaka, K. Chida, S. Matsuo, Y. Nishihara, D. Chiba, K. Kobayashi, T. Ono, A. Fukushima, and S. Yuasa, Low-frequency and shot noises in CoFeB/MgO/CoFeB magnetic tunneling junctions. *Phys. Rev. B* **86**, 224423 (2012).

[46] M. Sampietro, L. Fasoli, and G. Ferrari, Spectrum analyzer with noise reduction by cross-correlation technique on two channels. *Rev. Sci. Instrum.* **70**, 2520 (1999).

[47] I. Žutić, J. Fabian and S. Das Sarma, Spintronics: Fundamentals and applications. *Rev. Mod. Phys.* **76**, 323 (2004).

[48] L. Jiang, E. Nowak, P. Scott, J. Johnson, J. Slaughter, J. Sun, and R. Dave, Low-frequency magnetic and resistance noise in magnetic tunnel junctions. *Phys. Rev. B* **69**, 054407 (2004).

[49] R. Guerrero, F. G. Aliev, Y. Tserkovnyak, T. S. Santos, and J. S. Moodera, Shot Noise in Magnetic Tunnel Junctions: Evidence for Sequential Tunneling. *Phys. Rev. Lett.* **97**, 266602 (2006).

[50] K. Sekiguchi, T. Arakawa, Y. Yamauchi, K. Chida, M. Yamada, H. Takahashi, D. Chiba, K. Kobayashi and T. Ono, Observation of full shot noise in CoFeB/MgO/CoFeB-based magnetic tunneling junctions. *Appl. Phys. Lett.* **96**, 252504 (2010).

[51] J. Scola, H. Polovy, C. Fermon, M. Pannetier-Lecur, G. Feng, K. Fahy and J. M. D. Coey, Noise in MgO barrier magnetic tunnel junctions with CoFeB electrodes: Influence of annealing temperature. *Appl. Phys. Lett.* **90**, 252501 (2007).

[52] R. Guerrero, D. Herranz, F. G. Aliev, F. Greullet, C. Tiusan, M. Hehn and F. Montaigne, High bias voltage effect on spin-dependent conductivity and shot noise in carbon-doped Fe(001)/MgO(001)/Fe(001) magnetic tunnel junctions. *Appl. Phys. Lett.* **91**, 132504 (2007).

[53] K. Liu, K. Xia, and G. E. W. Bauer, Shot noise in magnetic tunnel junctions from first principles. *Phys. Rev. B* **86**, 020408(R) (2012).

[54] Cong Ren, Xiaoyong Liu, B. D. Schrag, and Gang Xiao, Low-frequency magnetic noise in magnetic tunnel junctions. *Phys. Rev. B* **69**, 104405 (2004).

[55] J. M. Almeida, R. Ferreira, P. P. Freitas, J. Langer, B. Ocker, and W. Maass, 1/f noise in linearized low resistance MgO magnetic tunnel junctions. *J. Appl. Phys.* **99**, 08B314 (2006).

[56] S. Ingvarsson, G. Xiao, S. S. P. Parkin, W. J. Gallagher, G. Grinstein, and R. H. Koch, Low-Frequency Magnetic Noise in Micron-Scale Magnetic Tunnel Junctions. *Phys. Rev. Lett.* **85**, 3289 (2000).

[57] F. G. Aliev, R. Guerrero, D. Herranz, R. Villar, F. Greullet, C. Tiusan, and M. Hehn, Very low 1/ f noise at room temperature in fully epitaxial Fe/MgO/Fe magnetic tunnel junctions. *Appl. Phys. Lett.* **91**, 232504 (2007).

[58] S. Ingvarssona, G. Xiao, R. A. Wanner, P. Trouilloud, Yu Lu, W. J. Gallagher, A. Marley, K. P. Roche, and S. S. P. Parkin, Electronic noise in magnetic tunnel junctions. *J. Appl. Phys.* **85**, 5270 (1999).

[59] R. Guerrero, F. G. Aliev, R. Villar, J. Hauch, M. Fraune, G. Gntherodt, K. Rott, H. Brückl, and G. Reiss, Low-frequency noise and tunneling magnetoresistance in Fe(110)/MgO(111)/Fe(110) epitaxial magnetic tunnel junctions. *Appl. Phys. Lett.* **87**, 042501 (2005).

[60] J. Scola, H. Polovy, C. Fermon, M. Pannetier-Lecoeur, G. Feng, K. Fahy, and J. M. D. Coey, Noise in MgO barrier magnetic tunnel junctions with CoFeB electrodes: Influence of annealing temperature. *Appl. Phys. Lett.* **90**, 252501 (2007).

[61] R. Stearrett, W. G. Wang, L. R. Shah, J. Q. Xiao, and E. R. Nowak, Magnetic noise evolution in CoFeB/MgO/CoFeB tunnel junctions during annealing. *Appl. Phys. Lett.* **97**, 243502 (2010).

[62] Aisha Gokce, E. R. Nowak, S. H. Yang and S. S. P. Parkin, 1/f noise in magnetic tunnel junctions with MgO tunnel barriers. *J. Appl. Phys.* **99**, 08A906 (2006).

[63] W. K. Park, J. S. Moodera, J. Taylor, M. Tondra, J. M. Daughton, Andy Thomas and Hubert Brückl, Noise properties of magnetic and nonmagnetic tunnel junctions. *J. Appl. Phys.* **93**, 7020 (2003).

[64] Y. Miura, S. Muramoto, K. Abe, and M. Shirai, First-principles study of tunneling magnetoresistance in Fe/MgAl$_2$O$_4$/Fe(001) magnetic tunnel junctions. *Phys. Rev. B* **86**, 024426 (2012).

[65] V. Drewello, J. Schmalhorst, A. Thomas, and G. Reiss, Evidence for strong magnon contribution to the TMR temperature dependence in MgO based tunnel junctions. *Phys. Rev. B* **77**, 014440 (2008).

[66] V. Drewello, M. Schäfers, O. Schebaum, A. A. Khan, J. Münchenberger, J. Schmalhorst, G. Reiss, and A. Thomas, Inelastic electron tunneling spectra of MgO-based magnetic tunnel junctions with different electrode designs. *Phys. Rev. B* **79**, 174417 (2009).

[67] J. M. Teixeira, J. Ventura, J. P. Araujo, J. B. Sousa, P. Wisniowski, S. Cardoso and P. P. Freitas, Resonant Tunneling through Electronic Trapping States in Thin MgO Magnetic Junctions. *Phys. Rev. Lett.* **106**, 196601 (2011).

[68] J. M. Teixeira, J. Ventura, J. P. Araujo, J. B. Sousa, P. Wisniowski and P. P. Freitas, Tunneling processes in thin MgO magnetic junctions. *Appl. Phys. Lett.* **96**, 262506 (2010).

[69] G. Iannaccone, F. Crupi, B. Neri and S. Lombardo, Theory and Experiment of Suppressed Shot Noise In Stress-Induced Leakage Currents. *IEEE Trans. Electron Devices* **50**, 1363 (2003).

[70] P. K. George, Y, Wu, R. M. White, E. Murdock and M. Tondra, Shot noise in low-resistance magnetic tunnel junctions. *Appl. Phys. Lett.* **80**, 682 (2002).

[71] J. G. Simmons, Generalized Formula for the Electric Tunnel Effect between Similar Electrodes Separated by a Thin Insulating Film. *J. Appl. Phys.* **34**, 1793 (1963).

[72] T. Shinjo, T. Okuno, R. Hassdorf, K. Shigeto and T. Ono, Magnetic Vortex Core Observation in Circular Dots of Permalloy. *Science* **289**, 930 (2000).

[73] O. Meplan, F. Brut and C. Gignoux, Tangent map for classical billiards in magnetic fields. *J. Phys. A* **26**, 237 (1993).

[74] 太田 恵造, 磁気工学の基礎 I—磁気の物理 共立全書 (1973).

[75] 高木 伸, 新物理学選書 巨視的トンネル現象 岩波書店 (1997).

[76] R. Zarzuela, S. Vélez, J. M. Hernandez, J. Tejada, and V. Novosad, Quantum depinning of the magnetic vortex core in micron-size permalloy disks. *Phys. Rev. B* **85**, 180401(R) (2012).

[77] M. A. Paalanen, D. C. Tsui, and A. C. Gossard, Quantized Hall effect at low temperatures. *Phys. Rev. B* **25**, 5566(R) (1982).

[78] K. von Klitzing, The quantized Hall effect. *Rev. Mod. Phys.* **58**, 519 (1986).

[79] B. I. Halperin, Statistics of Quasiparticles and the Hierarchy of Fractional Quantized Hall States. *Phys. Rev. Lett.* **52**, 1583 (1984).

[80] S. Tarucha, D. G. Austing, T. Honda, R. J. van der Hage, and L. P. Kouwenhoven, Shell Filling and Spin Effects in a Few Electron Quantum Dot. *Phys. Rev. Lett.* **77**, 3613 (1996).

[81] R. Hanson, L. P. Kouwenhoven, J. R. Petta, S. Tarucha and L. M. K. Vandersypen, Spins in few-electron quantum dots. *Rev. Mod. Phys.* **79**, 1217 (2007).

[82] C. M. Marcus, A. J. Rimberg, R. M. Westervelt, P. F. Hopkins, and A. C. Gossard, Conductance Fluctuations and Chaotic Scattering in Ballistic Microstructures. *Phys. Rev. Lett.* **69**, 506 (1992).

[83] K. J. Vahala, Optical microcavities. *Nature* **424**, 839 (2003).

[84] R. Ketzmerick, Fractal conductance fluctuations in generic chaotic cavities. *Phys. Rev. B* **54**, 10841 (1996).

[85] L. Christensson, H. Linke, P. Omling, P. E. Lindelof, I. V. Zozoulenko, and K.-F. Berggren, Classical and quantum dynamics of electrons in open equilateral triangular billiards. *Phys. Rev. B* **57**, 12306 (1998).

[86] 原山 卓久, 中村 勝弘, 量子カオス 量子ビリアードを舞台にして 培風館 (2000).

List of publications

1. Takahiro Tanaka, Tomonori Arakawa, Kensaku Chida, Yoshitaka Nishihara, Daichi Chiba, Kensuke Kobayashi, Teruo Ono, Hiroaki Sukegawa, Shinya Kasai, and Seiji Mitani, "Signature of Coherent Transport in Epitaxial Spinel-based Magnetic Tunnel Junctions Probed by Shot Noise Measurement", *Applied physics express* **5**, 0530003 (2012).

2. Takahiro Tanaka, Tomonori Arakawa, Masahiro Maeda, Kensuke Kobayashi, Yoshitaka Nishihara, Teruo Ono, Takayuki Nozaki, Akio Fukushima, and Shinji Yuasa, "Leak current estimated from the shot noise in magnetic tunneling junctions", *Applied Physics Letters* **105**, 042405 (2014).

3. Tomonori Arakawa, Takahiro Tanaka, Kensaku Chida, Sadashige Matsuo, Yoshitaka Nishihara, Daichi Chiba, Kensuke Kobayashi, Teruo Ono, Akio Fukushima, and Shinji Yuasa, "Low-frequency and shot noises in CoFeB/MgO/CoFeB magnetic tunneling junctions", *Physical Review B* **86**, 224423 (2012).

4. Kensaku Chida, Tomonori Arakawa, Sadashige Matsuo, Yoshitaka Nishihara, Takahiro Tanaka, Daichi Chiba, Teruo Ono, Tokuro Hata, Kensuke Kobayashi, Tomoki Machida, "Observation of finite excess noise in the voltage-biased quantum Hall regime as a precursor for breakdown", *Physical Review B* **87**, 235318 (2013).

5. Kensaku Chida, Tokuro Hata, Tomonori Arakawa, Sadashige Matsuo, Yoshitaka Nishihara, Takahiro Tanaka, Teruo Ono, and Kensuke Kobayashi, "Avalanche electron bunching in Corbino disk in quantum Hall effect breakdown regime", *Physical Review B* **89**, 235318 (2014).

6. Sadashige Matsuo, Shunpei Takeshita, Takahiro Tanaka, Shu Nakaharai, Kazuhito Tsukagoshi, Takahiro Moriyama, Teruo Ono, and Kensuke Kobayashi, "Edge Mixing Dynamics in Graphene $p - n$ Junctions in the Quantum Hall Regime", *Nature Communications* **6**, 8066 (2015).

List of presentation at international conferences

1. Takahiro Tanaka, Tomonori Arakawa, Kensaku Chida, Yoshitaka Nishihara, Daichi Chiba, Kensuke Kobayashi, Teruo Ono, Hiroaki Sukegawa, Shinya Kasai, and Seiji Mitani, "Spin-dependent Transport in Magnetic Tunneling Junctions Probed by the Shot Noise Measurement", Joint European Magnetic Symposia (JEMS 2012) (Parma, Italy, September 9-14, 2012) (poster).

2. Takahiro Tanaka, Tomonori Arakawa, Kensaku Chida, Yoshitaka Nishihara, Daichi Chiba, Teruo Ono, Masahiro Maeda, Kensuke Kobayashi, Takayuki Nozaki, Akio Fukushima, and Shinji Yuasa, "Barrier Thickness Dependence of the Shot Noise in the Epitaxial Fe/MgO/Fe Magnetic Tunneling Junctions", The 8th International Symposium on Metallic Multilayers (MML 2013) (Kyoto, Japan, May 19-24, 2013) (poster).

3. Takahiro Tanaka, Tomonori Arakawa, Masahiro Maeda, Yoshitaka Nishihara, Teruo Ono, Kensuke Kobayashi, Takayuki Nozaki, Akio Fukushima, and Shinji Yuasa, "Leak Current Contribution in Epitaxial Fe/MgO/Fe Magnetic Tunneling Junctions Determined by Shot Noise Measurement", International Magnetics Conference (INTERMAG 2014) (Dresden, Germany, May 4-8, 2014) (poster).

4. Takahiro Tanaka, Tomonori Arakawa, Masahiro Maeda, Kensuke Kobayashi, Yoshitaka Nishihara, Teruo Ono, Takayuki Nozaki, Akio Fukushima, and Shinji Yuasa, "Leak Current Contribution in Epitaxial Fe/MgO/Fe Magnetic Tunneling Junctions Determined by Shot Noise Measurement", The 1st International Symposium Interactive Materials Science Cadet Program (Osaka, Japan, November 16-19, 2014) (poster).

5. Takahiro Tanaka, Tomonori Arakawa, Masahiro Maeda, Yoshitaka Nishihara, Teruo Ono, Kensuke Kobayashi, Takayuki Nozaki, Akio Fukushima, and Shinji Yuasa, "Leak Current Contribution in Epitaxial Fe/MgO/Fe Magnetic Tunneling Junctions Determined by Shot Noise Measurement", International Symposium on Material Sciences (ISMS 2015) (Osaka, Japan, November 17 and 18, 2015) (poster)

List of presentation at the physical society of Japan meetings

1. 田中崇大, 荒川智紀, 知田健作, 西原禎孝, 千葉大地, 小林研介, 小野輝男, 介川裕章, 葛西伸哉, 三谷誠司 "スピネル型バリアを有するトンネル磁気抵抗素子におけるショット雑音" 日本物理学会 第 67 回年次大会 (関西学院大学 2012 年 3 月) (口頭)

2. 田中崇大, 荒川智紀, 知田健作, 西原禎孝, 千葉大地, 小林研介, 小野輝男, 介川裕章, 葛西伸哉, 三谷誠司 "スピネル型バリアを有するトンネル磁気抵抗素子におけるショット雑音" 日本物理学会 2012 年秋季大会 (横浜国立大学 2012 年 9 月) (ポスター)

3. 田中崇大, 荒川智紀, 知田健作, 西原禎孝, 千葉大地, 小野輝男, 前田正博, 小林研介, 野崎隆行, 福島章雄, 湯浅新治 "トンネル磁気抵抗素子におけるショット雑音の膜厚依存性" 日本物理学会 第 68 回年次大会 (広島大学 2013 年 3 月) (口頭)

4. 田中崇大, 荒川智紀, 田辺賢士, 小林研介, 小野輝男 "バリスティック検出器を用いた磁気渦コアの極性検出の試み" 日本物理学会 2013 年秋季大会 (徳島大学 2013 年 9 月) (ポスター)

5. 田中崇大, 荒川智紀, 前田正博, 西原禎孝, 小野輝男, 小林研介, 野崎隆行, 福島章雄, 湯浅新治 "トンネル磁気抵抗素子におけるショット雑音の膜厚依存性" 日本物理学会 第 69 回年次大会 (東海大学 2014 年 3 月) (口頭)

6. 田中崇大, 荒川智紀, 田辺賢士, 小林研介, 小野輝男 "SQUID を用いた磁気渦の極性反転検出の試み" 日本物理学 2014 年秋季大会 (中部大学 2014 年 9 月) (ポスター)

7. 田中崇大, 河村智哉, 荒川智紀, 田辺賢士, 小林研介, 山田啓介, 仲谷栄伸, 小野輝男 "バリスティック検出器を用いた磁気渦コアの極性検出の可能性" 日本物理学会第 70 回年次大会 (早稲田大学 2015 年 3 月) (口頭)